N-WASP-dependent branched actin polymerization attenuates B-cell receptor signaling by increasing the molecular density of receptor clusters

Anshuman Bhanja[1†], Margaret K. Seeley-Fallen[1], Michelle Lazzaro[1^], Arpita Upadhyaya[2,3,4], and Wenxia Song[1]*

[1]Department of Cell Biology and Molecular Genetics, University of Maryland, College Park, MD 20742, USA

[2]Biophysics Program, University of Maryland, College Park, MD, 20742, USA.

[3]Department of Physics, University of Maryland, College Park, MD, 20742, USA. arpitau@umd.edu.

[4]Institute for Physical Science and Technology, University of Maryland, College Park, MD, 20742, USA.

[†]Current address: Department of Pharmacology, University of California, San Diego, CA, 92034, USA

[^] Current address: AstraZeneca, Gaithersburg, MD 20878, United States

[*] Authors for correspondence: wenxsong@umd.edu and arpitau@umd.edu

Abstract

Antigen-induced B-cell receptor (BCR) signaling is critical for initiating and regulating B-cell activation. The actin cytoskeleton plays essential roles in BCR signaling. Upon encountering cell-surface antigens, actin-driven B-cell spreading amplifies signaling, while B-cell contraction following spreading leads to signal attenuation. However, the mechanism by which actin dynamics switch BCR signaling from amplification to attenuation is unknown. Here, we show that Arp2/3-mediated branched actin polymerization is required for B-cell contraction. Contracting B-cells generate centripetally moving actin foci from lamellipodial F-actin networks in the B-cell plasma membrane region contacting antigen-presenting surfaces. Actin polymerization driven by N-WASP, but not WASP, initiates these actin foci and facilitates non-muscle myosin II recruitment to the contact zone, creating actomyosin ring-like structures. Furthermore, B-cell contraction increases BCR molecular density in individual clusters, leading to decreased BCR phosphorylation. Increased BCR molecular density reduced levels of the stimulatory kinase Syk, the inhibitory phosphatase SHIP-1, and their phosphorylated forms in individual BCR clusters. These results suggest that N-WASP-activated Arp2/3, coordinating with myosin, generates centripetally moving foci and contractile actomyosin ring-like structures from lamellipodial networks, enabling contraction. B-cell contraction attenuates BCR signaling by pushing out both stimulatory kinases and inhibitory phosphatases from BCR clusters, providing novel insights into actin-facilitated signal attenuation.

42 ## Introduction

43 B-cell-mediated antibody responses are essential for eliminating invading pathogens. B-cell
44 receptors (BCRs) expressed on the B-cell surface detect the presence of cognate antigens. The
45 binding of antigen to the BCR leads to the activation of signaling cascades (Reth and Wienands
46 1997; Dal Porto *et al.* 2004; Kwak *et al.* 2019), which induce transcriptional programs that
47 prepare B-cells for proliferation and differentiation (Kurosaki *et al.* 2010; Shlomchik *et al.* 2019;
48 Wang *et al.* 2020). BCR signaling also induces rapid antigen internalization, processing, and
49 presentation for T-cell recognition, which provides the second signal required for B-cell clonal
50 expansion and differentiation to high-affinity antibody-secreting cells and memory B-cells (Song
51 *et al.* 1995; Gitlin *et al.* 2014). BCR signaling is tightly regulated by various external and internal
52 factors to activate antibody responses that are specific and also qualitatively and quantitatively
53 matched to the encountered antigen.
54
55 Antigen-induced receptor reorganization activates BCRs at the B-cell surface. Antigen binding
56 leads to BCR clustering at lipid rafts, which enables raft-resident kinases, such as the Src
57 kinases Lyn and Fyn, to phosphorylate immunoreceptor tyrosine-based activation motifs
58 (ITAMs) in the cytoplasmic domains of the BCR signaling subunit CD79a/b heterodimer (Reth
59 1994; Pierce 2002; Sohn *et al.* 2008). Doubly phosphorylated ITAMs recruit and activate spleen
60 tyrosine kinase (Syk), which in turn activates multiple downstream signaling pathways, including
61 phospholipase Cγ2 (PLCγ2), Bruton's tyrosine kinase (Btk), Ras-GTPase, and
62 phosphatidylinositol-3 kinase (PI3K), initiating signaling cascades (Kurosaki 2000; Dal Porto *et*
63 *al.* 2004; Tanaka and Baba 2020). Signaling activation also induces the recruitment and
64 activation of inhibitory phosphatases, such as SH2-containing tyrosine phosphatase-1 (SHP-1)
65 and phosphatidylinositol-5 phosphatase-1 (SHIP-1), to BCR signaling complexes (Brauweiler *et*
66 *al.* 2000; Gross *et al.* 2009; Franks and Cambier 2018). SHIP-1 and SHP-1 negatively regulate

67 BCR signaling by inactivating the plasma membrane docking lipids for stimulatory kinases, such
68 as Btk and Akt (Aman *et al.* 1998; Bolland *et al.* 1998) and dephosphorylating BCR and its
69 downstream signaling molecules (Mizuno *et al.* 2000; Adachi *et al.* 2001), respectively. The
70 interplay between the stimulatory kinases and the inhibitory phosphatases controls the balance
71 of antibody responses against pathogens and self. Deficiencies in stimulatory kinases by
72 mutations, such as Btk, cause X-linked agammaglobulinemia (XLA) (Kinnon *et al.* 1993), while
73 deficiencies in the inhibitory phosphatases SHP-1 or SHIP-1 result in autoimmune diseases
74 (Pao *et al.* 2007; Leung *et al.* 2013). However, the mechanisms by which BCR signaling
75 attenuation is initiated and regulated remain elusive.
76
77 B-cells encounter both soluble and membrane-associated antigens *in vivo*. Membrane-
78 associated antigens include antigens on antigen-presenting cells, like follicular dendritic cells in
79 B-cell follicles or germinal centers, and pathogenic cells, like bacteria, parasites, and cancer
80 cells (Batista and Harwood 2009; Depoil *et al.* 2009; Gonzalez *et al.* 2009; Cyster 2010). The
81 binding of multi-valent soluble antigen and membrane-associated antigen with any valency
82 induces dynamic reorganization of surface BCRs into microclusters, triggering BCR signaling.
83 Subsequently, surface BCRs continue moving to the plasma membrane region contacting
84 antigen-presenting surfaces or to one B-cell pole in the case of soluble antigen, which leads to
85 the growth and merger of BCR microclusters and the formation of immunological synapses
86 (Carrasco *et al.* 2004; Harwood and Batista 2010) or supra-molecular activation complexes
87 (Unanue and Karnovsky 1973; Schreiner and Unanue 1977; Tolar *et al.* 2009b; Harwood and
88 Batista 2010).
89
90 Multiple mechanisms have been proposed for signaling initiation by antigen-induced surface
91 BCR reorganization. The binding of surface BCRs to membrane-associated antigen has been
92 shown to induce a conformational change in the BCR extracellular domain, exposing a proximal

membrane region of membrane IgM that promotes receptor clustering (Tolar *et al.* 2009a; Shen *et al.* 2019). Antigen-binding also changes the conformation of the BCR cytoplasmic domains from a closed to an open form, facilitating the recruitment of signaling molecules (Tolar *et al.* 2005). Alternatively, antigen-BCR interaction can increase the molecular spacing of BCRs in clusters, facilitating BCR interaction with signaling molecules (Yang and Reth 2010; Kläsener *et al.* 2014). The inhibitory phosphatases SHP-1 and SHIP-1 are also recruited to BCR clusters (Adachi *et al.* 2001; Seeley-Fallen *et al.* 2014). However, the mechanisms underlying phosphatase recruitment and its relationship with BCR signaling activation complexes are unknown.

The actin cytoskeleton is essential for antigen-induced BCR reorganization on the B-cell surface in response to both soluble and membrane-associated antigen (Harwood and Batista 2011; Liu *et al.* 2013b; Song *et al.* 2013; Hoogeboom and Tolar 2016). Early signaling of the BCR triggers transient actin depolymerization via Rap GTPase and its downstream target cofilin (Freeman *et al.* 2011), which disassembles the existing cortical actin network that confines the lateral movement of surface BCRs (Treanor *et al.* 2010). Following this transient depolymerization, BCR signaling activates rapid actin polymerization through the actin nucleation promoting factors Wiskott-Aldrich Syndrome Protein (WASP) and neuronal-WASP (N-WASP), modulating BCR mobility and leading to F-actin accumulation at BCR-antigen interaction sites (Liu *et al.* 2013a; Rey-Suarez *et al.* 2020). Actin polymerization and treadmilling in B-cells stimulated by soluble antigen drive surface BCRs to cluster and move to one pole of the B-cell, forming a BCR cap (Schreiner and Unanue 1977; Liu *et al.* 2012a). Upon interacting with membrane-associated antigen, B-cells organize actin into two dynamic structures. One treadmills outwards, driving B-cell membrane spreading and expanding the B-cell membrane region contacting the antigen-presenting surface (contact zone), which enables more BCRs to engage antigen (Bolger-Munro *et al.* 2019). The other creates retrograde flow towards the center of the B-cell contact zone,

119 driving the centripetal movement and growth of BCR microclusters (Liu *et al.* 2012b). Together,
120 these processes amplify BCR signaling (Batista *et al.* 2010; Harwood and Batista 2011). The
121 extent of B-cell spreading and the amount of BCR-antigen complexes gathered in the contact
122 zone depend on BCR binding affinity and the density of antigen on the membrane (Fleire *et al.*
123 2006). Subsequent to spreading, B-cells contract, reducing the contact area, which drives BCR
124 microclusters to merge into central clusters to form immunological synapses (Fleire *et al.* 2006;
125 Liu *et al.* 2013a).
126
127 The actin cytoskeleton closely interplays with BCR signaling. We have previously shown that
128 mouse primary B-cells with Btk deficiency (Liu *et al.* 2011) or double knockouts of the actin
129 nucleation promoting factors WASP and N-WASP (Liu *et al.* 2013a) fail to spread on antigen-
130 presenting surfaces and establish stable interactions with membrane-associated antigen,
131 drastically reducing BCR signaling. Btk can activate WASP and N-WASP through Vav, the
132 guanine nucleotide exchange factor of Cdc42 and Rac and phosphatidylinositol-5 kinase that
133 generates phosphatidylinositol-4,5-biphosphate (PI4,5P_2) (Sharma *et al.* 2009; Padrick and
134 Rosen 2010). Surprisingly, B-cell-specific knockout of N-WASP (cNKO) but not WASP germline
135 knockout (WKO) enhances B-cell spreading, delays B-cell contraction, and inhibits the
136 centralization of BCR clusters at the contact zone (Liu *et al.* 2013a). Consistent with these
137 findings, Bolger-Munro et al. have shown that knockdown of the actin nucleation factor Arp2/3
138 downstream of WASP and N-WASP disrupts the dynamic actin reorganization induced by
139 membrane-associated antigen required for BCR microcluster growth and merger (Bolger-Munro
140 *et al.* 2019). Using B-cell-specific and germline knockouts, we showed that in addition to N-
141 WASP, the actin motor non-muscle myosin IIA (NMIIA) (Seeley-Fallen *et al.* 2022) and the
142 actin-binding adaptor protein Abp1 (Seeley-Fallen *et al.* 2014) are required for B-cell contraction
143 and BCR central cluster formation. Finally, Wang et al. recently showed that in the presence of
144 the adhesion molecule ICAM on the antigen-presenting surface, B-cells form contractile

145 actomyosin arcs, driving centripetal movement of BCR clusters in the B-cell contact zone (Wang
146 *et al.* 2022). Together, these findings indicate a critical role of different actin networks in B-cell
147 contraction and BCR signaling.
148
149 Our previous studies demonstrate that B-cell contraction is critical for BCR signaling
150 attenuation. Delay or inhibition of B-cell contraction due to deficiencies in actin regulators, N-
151 WASP, Abp1, or NMIIA, prolongs and/or increases BCR signaling by enhancing the activation of
152 stimulatory kinases and suppressing the activation of inhibitory phosphatases, which elevates
153 the production of autoantibody levels in mice (Liu *et al.* 2013a; Seeley-Fallen *et al.* 2014;
154 Seeley-Fallen *et al.* 2022). N-WASP and NMIIA are not known to interact with kinases and
155 phosphatases directly. The growth, merger, and centralization of antigen-BCR complexes at the
156 B-cell contact zone during the B-cell contraction phase are associated with reduced BCR
157 signaling capability (Liu *et al.* 2013a). These findings suggest that B-cell contraction is one of
158 the mechanisms for inducing BCR signaling attenuation. However, how the actin cytoskeleton
159 facilitates the transition of the spreading to contraction phase and how B-cell contraction
160 switches BCR signaling from amplification to attenuation is unknown.
161
162 This study explores the mechanisms by which the actin cytoskeleton remodels from spreading
163 lamellipodia to contractile structures and by which B-cell contraction suppresses BCR signaling.
164 Our results show that the contractile actomyosin structures responsible for B-cell contraction
165 originate from branched actin at spreading lamellipodia. N-WASP/Arp2/3- mediated actin
166 polymerization prolongs the lifetime of the lamellipodial actin structures, enables NMIIA
167 recruitment, and drives their movement to the center of the B-cell contact zone. B-cell
168 contraction increases the molecular density within individual BCR-antigen clusters, which
169 promotes the disassociation of both the stimulatory kinase Syk and the inhibitory phosphatases

170 SHIP-1 from BCR clusters, leading to signal attenuation. Our study reveals a new mechanism
171 underlying BCR signal downregulation.
172
173 **Results**
174 **Arp2/3, activated by N-WASP but not WASP, is required for B-cell contraction**
175 Arp2/3-generated branched F-actin is known to drive lamellipodial expansion for B-cell
176 spreading (Bolger-Munro *et al.* 2019). However, whether branched F-actin is involved in the
177 subsequent contraction phase is unknown. To address this, we perturbed the polymerization of
178 branched F-actin using the Arp2/3 inhibitor CK-666 (50 μM) while using its inactive derivative
179 CK-689 as a control. Pre-warmed splenic B-cells from WT C57BL/6 mice were incubated with
180 monobiotinylated Fab' fragment of anti-mouse IgM+G attached to planar lipid bilayers (Fab'-
181 PLB) by biotin-streptavidin interaction and imaged live at 37°C using interference reflection
182 microscopy (IRM). The contact area of B-cells treated with CK-689 rapidly increased upon
183 contacting Fab'-PLB and reached a maximum at ≥0.5 min after the initial contact (*Figure 1A,*
184 *Figure 1-figure supplement 1, and Figure 1-Video 1A*). Following maximal spreading, most B-
185 cells reduced the area of their contact zone, indicating contraction (*Figure 1A, Figure 1-figure*
186 *supplement 1, and Figure 1-Video 1A*). We classified a B-cell as contracting if its contact zone
187 area reduced by ≥5% for at least 10 sec after reaching a maximum value. Based on the average
188 timing for B-cell maximal spreading, we treated B-cells with CK-666 at the beginning of the
189 incubation (Time 0), before B-cell spreading initiation, or at 2 min, when all B-cells had already
190 spread. The effectiveness of CK-666 was detected by reduced Arp2/3 staining in the contact
191 zone (*Figure 1-figure supplement 2*). As expected, CK-666 treatment at 0 but not 2 min reduced
192 the kinetics of B-cell spreading (*Figure 1-figure supplement* 3). Importantly, CK-666 treatment at
193 0 and 2 min both significantly reduced the percentage of B-cells undergoing contraction (*Figure*
194 *1A-C and Figure 1-Video 1A*). The inhibitory effect of CK-666 on B-cell contraction, particularly

195 CK-666 treatment after B-cell spreading, suggests that Arp2/3-mediated branched actin
196 polymerization is required for B-cell contraction.
197
198 WASP and N-WASP are actin nucleation-promoting factors upstream of Arp2/3 that are
199 expressed in B-cells (Padrick and Rosen 2010). To determine if either or both were responsible
200 for activating Arp2/3 for B-cell contraction, we utilized the N-WASP inhibitor wiskostatin (Wisko),
201 and splenic B-cells from B-cell-specific N-WASP knockout mice (cNKO) and germline WASP
202 knockout (WKO) mice (Westerberg *et al.* 2012; Liu *et al.* 2013a). Wisko has been shown to
203 inhibit N-WASP activation while enhancing WASP activation in B-cells (*Figure 1-figure*
204 *supplement 4*) (Liu *et al.* 2013a). We found that both Wisko (10 μM) (*Figure 1D and E and*
205 *Figure 1-Video 1B*) and cNKO (*Figure 1F and G and Figure 1-Video 1C*), but not WKO (*Figure*
206 *1H and I and Figure 1-Video 1D*), significantly reduced the percentage of B-cells undergoing
207 contraction, compared to the vehicle, flox, or WT controls. These results suggest that N-WASP-
208 but not WASP-activated Arp2/3 mediates branched actin polymerization for B-cell contraction.
209
210 **Arp2/3, downstream of N-WASP, generates inner F-actin foci, driving B-cell contraction**
211 To understand how Arp2/3 drives B-cells to transition from spreading to contraction, we
212 identified F-actin structures associated with contracting B-cells that were sensitive to CK-666
213 treatment. We visualized F-actin by phalloidin staining and compared F-actin organization in the
214 contact zone of B-cells at the spreading (2 min) and contraction (4 min) phases using TIRF.
215 While B-cells in both spreading and contraction phases exhibited phalloidin staining outlining the
216 contact zone (*Fig. 2A, green arrows*), only B-cells in the contracting phase showed interior
217 phalloidin patches brighter than the phalloidin staining at the periphery of the contact zone
218 (*Figure 2A, purple arrows*). These F-actin patches were organized into a ring-like structure and
219 resided ~1 μm behind the spreading front, surrounding an F-actin-poor center (*Figure 2A, purple*
220 *arrows*). Here, we refer these F-actin patches as inner F-actin foci. We identified inner F-actin

221 foci based on whether their peak fluorescence intensity (FI) was ≥2 fold of the mean
222 fluorescence intensity (MFI) of phalloidin in the no-foci area, had diameters of ≥250 nm, and
223 were located 1 μm away from the edge of the contact zone. We found that such inner F-actin
224 foci were detected in >60% of B-cells in the contracting phase (4 min) but only in <20% of B-
225 cells in the spreading phase (2 min) (*Figure 2B*). CK-666 treatment at 0 min, which inhibited B-
226 cell contraction, significantly reduced the percentage of B-cells showing inner F-actin foci at 4
227 min but not at 2 min (*Figure 2B*). CK-666 treatment did not affect the phalloidin staining outlining
228 the contact zone (*Figure 2A*). Similarly, the percentage of cNKO B-cells showing inner F-actin
229 foci was drastically reduced at 4 min but not at 2 min (*Figure 2C*). These results suggest that the
230 formation of these inner F-actin foci is associated with B-cell contraction.
231
232 We further quantified the number of inner F-actin foci in individual B-cells from mice expressing
233 the LifeAct-GFP transgene (Riedl *et al.* 2010) (*Figure 2D, E, and G*), which allowed us to
234 monitor F-actin reorganization using live-cell imaging (*Figure 2-Video 1*), or using phalloidin
235 staining in flox control and cNKO B-cells (*Figure 2F*). Consistent with the results with phalloidin
236 staining, CK-666 treatment at time 0 significantly reduced the number of inner F-actin foci in the
237 contact zone (*Figure 2D and Figure 1-Video 1A and B*). When we followed the same B-cells
238 before and after CK-666 treatment at 2 min, many of the inner F-actin foci formed before the
239 treatment (1 min 50 sec) disappeared after the treatment (2 min 20 sec), significantly reducing
240 the number of inner F-actin foci (*Figure 2E*). Similar to the CK-666 treatment, cNKO cells
241 significantly reduced the number of inner F-actin foci in the contact zone, compared to flox
242 controls (*Figure 2F*). In contrast, WKO, which does not affect B-cell contraction, did not
243 significantly change the number of inner F-actin foci, compared to WT control B-cells (*Figure 2G*
244 *and Figure 2-Video 1C and D*). Thus, N-WASP- but not WASP-activated Arp2/3 drives the
245 formation and the maintenance of contraction-associated inner F-actin foci.
246

247 **Inner F-actin foci are derived from lamellipodial actin networks supporting the spreading**
248 **membrane**
249 We next examined the formation of contraction-associated inner F-actin foci utilizing live-cell
250 TIRF imaging of B-cells from mice expressing LifeAct-GFP. We generated kymographs along
251 eight lines from the center of each contact zone using time-lapse images of LifeAct-GFP (*Figure*
252 *3A and B and Figure 3-figure supplement 1*). Analysis of these kymographs showed that most
253 F-actin foci were first detected closely behind lamellipodial F-actin networks. Following maximal
254 spreading, these F-actin foci moved centripetally while increasing in intensity, becoming inner F-
255 actin foci, in cells transitioning from spreading to contraction (*Figure 3B, top panel, and Figure*
256 *3-figure supplement 1*). However, such centripetally moving F-actin foci were not detected in B-
257 cells that did not undergo contraction (*Figure 3B, bottom panel*). We quantified the percentage
258 of the eight kymographs from each cell that exhibited lamellipodia-derived inner F-actin foci and
259 found, on average, that six out of eight kymographs from contracting cells showed lamellipodia-
260 derived inner F-actin foci, compared to only one or two kymographs from non-contracting cells
261 (*Figure 3C*). To examine the temporal relationship between the generation of lamellipodia-
262 derived inner F-actin foci and contraction, we plotted the percentage of kymographs with
263 lamellipodia-derived inner F-actin foci over time with the spreading to contracting transition time
264 set as 0 (*Figure 3D*). We found that the percentage of kymographs showing lamellipodia-derived
265 inner F-actin foci peaked at almost the same time when the spreading transitioned to
266 contraction (*Figure 3D*), suggesting a close temporal relationship between the two events.
267 Furthermore, the N-WASP inhibitor Wisko, but not WKO, significantly inhibited the formation of
268 lamellipodia-derived inner F-actin foci (*Figure 3E*). Thus, inner F-actin foci originate from
269 branched actin driven lamellipodia and form simultaneously with the transition of B-cell
270 spreading to contraction.
271

272 **N-WASP-activated Arp2/3 generates inner F-actin foci by sustaining the lifetime and the**
273 **centripetal movement of lamellipodial F-actin**
274 We examined the mechanism by which N-WASP and Arp2/3 generate inner F-actin foci by
275 measuring their relative lifetime and mobility using kymographs generated from TIRF time-lapse
276 images of B-cells expressing LifeAct-GFP. Inner F-actin foci were identified as described above,
277 and their tracks were manually determined (*Figure 4A, black dashed lines*). The time window in
278 which an inner F-actin patch could be detected in a kymograph was measured as the relative
279 lifetime, as actin foci could move away from the kymograph line or the TIRF evanescent field
280 (*Figure 4A, right panels*). The distance each F-actin focus moved during its lifetime was used to
281 calculate its speed (*Figure 4A, right panels*). Compared to CK-689-treated B-cells, CK-666
282 treatment at time 0 significantly reduced the relative lifetime and the centripetal speed of inner
283 F-actin foci (*Figure 4B-D*). After B-cells were treated with CK-666 at 2 min (the average time for
284 B-cells to reach the maximal spreading), the relative lifetime and the centripetal speed of inner
285 F-actin foci were significantly lower than before the treatment in the same cell (*Figure 4E-G,*
286 *line-linked dots*). Similarly, the N-WASP inhibitor Wisko significantly reduced the relative lifetime
287 and the centripetal speed of inner F-actin foci (*Figure 4H-J*); however, WKO had no significant
288 effect (*Figure 4K-M*). These results show that N-WASP and Arp2/3 mediated branched actin
289 polymerization prolongs the lifetime of lamellipodia-derived F-actin foci and drives them to move
290 inward in the B-cell contact zone.
291
292 **N-WASP coordinates with NMII to generate inner actin foci and NMII ring-like structures**
293 As non-muscle myosin II (NMII) is required for B-cell contraction (Seeley-Fallen *et al.* 2022), we
294 examined the relationship between the formation of inner F-actin foci and the recruitment and
295 reorganization of NMII in the contact zone using TIRF imaging of B-cells from mice expressing a
296 GFP-NMIIA transgene. Upon interacting with Fab'-PLB, the GFP-NMIIA MFI in the contact zone
297 of untreated WT B-cells increased rapidly in the first minute and slowly afterward (*Figure 5A and*

298 *B and Figure 5-Video 1*). Wiskostatin treatment significantly reduced the GFP-NMIIA MFI in the
299 contact zone (*Figure 5B*) and its initial rate of increase (as determined by the slope of the GFP-
300 NMIIA MFI increase at 0~30 sec time window) (*Figure 5C*). Kymographs generated from time-
301 lapse TIRF images of B-cells from mice expressing GFP-NMIIA and LifeAct-RFP showed that
302 recruited NMIIA accumulated between lamellipodia and inner F-actin foci when the foci moved
303 centripetally away from lamellipodia (*Figure 5D, white arrow, and Figure 5-Video 1*). Recruited
304 NMIIA reorganized with inner F-actin foci to form a ring-like structure in the contact zone (*Figure*
305 *5A, D, and E, and Figure 5-Video 1*). The percentage of B-cells with NMIIA ring-like structures,
306 visualized by immunostaining, increased over time as more B-cells underwent contraction
307 (*Figure 5E and F*). Compared to flox controls, the percentage of cNKO B-cells with NMIIA ring-
308 like structures was significantly decreased (*Figure 5E and F*). Wiskostatin treatment also
309 reduced NMIIA recruitment and ring-like structure formation (*Figure 5-Video 1*). Surprisingly, the
310 percentage of WKO B-cells with NMIIA ring-like structure was higher than that of flox control B-
311 cells (*Figure 5E and F*). Thus, N-WASP and Arp2/3 mediated branched actin polymerization
312 promotes the recruitment and the reorganization of NMII ring-like structures.
313
314 We next tested whether recruited NMII contributed to the formation of inner actin foci by
315 inhibiting its motor activity using blebbistatin, which is known to impede B-cell contraction
316 (Seeley-Fallen *et al.* 2022). Inner F-actin foci in the B-cell contact zone were identified by
317 phalloidin staining, as described in Figure 2. Treatment with blebbistatin significantly reduced
318 the percentages of WT splenic B cells exhibiting inner F-actin foci ring-like structures (*Figure 5G*
319 *and H*). This result suggests that while NMII is recruited with the help of N-WASP and Arp2/3
320 mediated actin polymerization, its motor activity is critical for the maturation of F-actin structures
321 associated with B-cell contraction.
322
323 **B-cell contraction increases the BCR molecular density in individual clusters**

324 To understand how B-cell contraction promotes BCR signaling attenuation, we examined the
325 impact of B-cell contraction on the properties of BCR clusters. We first measured the MFI of
326 AF546-Fab' attached to PLB gathered by B-cells into the contact zone as an indication of the
327 overall BCR molecular density. The clustering of AF546-Fab' on PLB by B-cell binding reflects
328 surface BCR clustering, as B-cell binding to transferrin (Tf)-tethered PLB does not cause
329 surface BCRs to cluster and be phosphorylated (*Figure 6-figure supplement 1*) (Liu *et al.* 2011;
330 Liu *et al.* 2013a). The MFI of AF546-Fab' in the B-cell contact zone increased over time.
331 Treatment with CK-666, Wisko, or cNKO all reduced the AF546-Fab' MFI, particularly during the
332 time window of B-cell contraction in controls (*Figure 6A-G, purple rectangles, and Figure 6-*
333 *Video 1*). Notably, the rates of increase in AF546-Fab' MFI, calculated from the slopes of
334 AF546-Fab' MFI versus time plots in individual cells, were significantly higher during B-cell
335 contraction than before B-cell contraction in control cells and conditions (*Figure 6D-K*).
336 Significantly, inhibiting B-cell contraction by CK-666 treatment at 0 (*Figure 6A, D, and H, and*
337 *Figure 6-Video 1A and D*) or 2 min (*Figure 6A, E, and I*), Wisko (*Figure 6B, F, and J, and Figure*
338 *6-Video 1B and E*), and cNKO (*Figure 6C, G, and K, and Figure 6-Video 1C and F*) reduced the
339 increases in AF546-Fab' accumulation rates. We further examined the peak FI of AF546-Fab' in
340 individual microclusters as a measure of the BCR molecular density in individual clusters.
341 AF546-Fab' clusters were identified based on their diameters ≥250 nm, peak FI ≥1.1 fold
342 outside the B-cell contact zone, and trackable for ≥20 sec (*Figure 6L and Figure 6-figure*
343 *supplement 2*). AF546-Fab' microclusters could not be identified during the early stage of B-cell
344 spreading. Time-lapse imaging by TIRF enabled us to measure the rate of increase in AF546-
345 Fab' peak FI in individual clusters (*Figure 6M and Figure 6-figure supplement 2*). Consistent
346 with our observation of AF546-Fab' MFI increase in the contact zone, the peak FI of individual
347 clusters increased at a faster rate during contraction than after contraction (when the contact
348 area no longer decreased) (*Figure 6N*). Furthermore, CK-666 (*Figure 6O*), Wisko (*Figure 6P*),
349 and cNKO (*Figure 6Q*) all significantly reduced the rate of increase in AF546-Fab' peak FI in

350 individual clusters. These results show that B-cell contraction significantly increases the
351 molecular density of BCRs in BCR clusters.
352
353 **Increased BCR molecular density by B-cell contraction reduces BCR phosphorylation**
354 **levels in individual microclusters**
355 To examine how BCR molecular density influenced BCR signaling capability, we
356 immunostained B-cells interacting with AF546-Fab'-PLB for 1, 3, 5, and 7 min, for
357 phosphorylated CD79a (pCD79a, Y182) and performed IRM and TIRF imaging (*Figure 7A and*
358 *H*). We analyzed equal numbers of AF546-Fab' clusters selected randomly, in the contact zone
359 of B-cells interacting with Fab'-PLB for 1, 3, 5, and 7 min, using a gradient threshold of their
360 AF546-Fab' MFI, 1.1 to 4.1 fold of the background, and with diameter ≥250 nm (*Figure 6-figure*
361 *supplement 2*). We determined the MFI of pCD79a and AF546-Fab' in individual clusters and
362 plotted the MFI ratio of pCD79a relative to AF546-Fab' (reflecting the relative level of BCR
363 phosphorylation) versus the AF546-Fab' peak FI (reflecting BCR molecular density) in individual
364 clusters (*Figure 7B and C*). The dot plots show that individual AF546-Fab' clusters with relatively
365 low peak FI displayed increasing MFI ratios of pCD79a to AF546-Fab' as the AF546-Fab' peak
366 FI rose in flox control B-cells (*Figure 7B*). Past a certain level of AF546-Fab' peak FI, the MFI
367 ratios of pCD79a to AF546-Fab' decreased as the AF546-Fab' peak FI in individual clusters
368 further increased (*Figure 7A and B*). Inhibition of B-cell contraction by cNKO reduced the
369 AF546-Fab' peak FI in individual clusters, maintaining it within a relatively low range, where the
370 MFI ratios of pCD79a to AF546-Fab' increased with the AF546-Fab' peak FI (*Figure 7C and D*).
371 Additionally, the average pCD79a to Fab' MFI ratios were much higher in cNKO B-cells than flox
372 control B-cells, when comparing AF546-Fab' clusters with the same range of peak FI (*Figure*
373 *7B-D*). During the contraction stage (5 and 7 min), flox control B-cells exhibited increased
374 AF546-Fab' MFI (*Figure 7E*) but decreased pCD79a MFI (*Figure 7F*) and the MFI ratios of
375 pCD79a relative to AF54-Fab' (*Figure 7G*) in individual clusters, compared to the spreading

376 stage (1 and 3 min). In contrast, non-contracting cNKO B-cells only slightly increased AF546-
377 Fab' MFI (*Figure 7E*) but significantly increased pCD79a MFI (*Figure 7F*) and the pCD79a to
378 AF546-Fab' MFI ratios (*Figure 7G*) in individual clusters at the contraction stage compared to
379 the spreading stage. Consequently, individual clusters in non-contracting cNKO B-cells had
380 significantly lower AF546-Fab' MFI but significantly higher pCD79a MFI and pCD79a to AF546-
381 Fab' FIRs than contracting flox control B-cells at 5 and 7 min but not at 1 and 3 min (*Figure 7E-*
382 *G*). Similarly, inhibiting B-cell contraction by treatment with the Arp2/3 inhibitor CK-666 at 2 min
383 post-stimulation reduced AF546-Fab' MFI (*Figure 7I*) but increased pCD79a MFI (*Figure 7J*)
384 and the MFI ratios of pCD79a relative to AF546-Fab' (*Figure 7K*) in individual clusters. These
385 data suggest that increases in BCR molecular density in BCR clusters during B-cell contraction
386 inhibit BCR phosphorylation.
387
388 **Increased BCR molecular density by B-cell contraction promotes the disassociation of**
389 **the stimulatory kinase Syk from BCR microclusters**
390 Increased BCR molecular density may promote signaling attenuation by inducing the
391 disassociation and/or dephosphorylation of stimulatory kinases from and at BCR clusters. To
392 test this hypothesis, we analyzed the relative amounts of Syk, a major stimulatory kinase in the
393 BCR signaling pathway, and its phosphorylated form pSyk (Y519/520) in individual BCR
394 clusters in relation to the molecular density of BCRs. Splenic B-cells were incubated with Fab'-
395 PLB for 3 and 7 min (when most cells were at the spreading and contraction phase,
396 respectively), fixed, permeabilized, stained for Syk (*Figure 8A*) or pSyk (*Figure 8E*), and imaged
397 using TIRF. We measured MFI ratios of Syk relative to AF546-Fab' in individual BCR clusters to
398 reflect the relative amount of Syk associated with individual BCR clusters and analyzed their
399 relationship with AF546-Fab' peak FI (reflecting the molecular density within BCR clusters).
400 AF546-Fab' clusters were detected and analyzed as described above. In flox control B-cells, the
401 highest fractions of BCR clusters had an AF546-Fab' peak FI at the150~200 range (*Figure 8A,*

402 *top panels, and Figure 8B, brown line and symbol*s). The average MFI ratios of Syk to Fab' in
403 individual clusters increased at a low peak FI range (<140) and did not significantly decrease
404 until Fab' peak FI reached a relatively high range (>280) (*Figure 8B, black line and symbol*). B-
405 cells from cNKO mice exhibited a reduction in the Fab' peak FI of clusters (*Figure 8A, bottom*
406 *panels, and Figure 8C and D, brown line and symbol*) but an increase in the average Syk to
407 Fab' MFI ratios in clusters in a wide range of Fab' peak FI, when compared to flox control B-
408 cells (*Figure 8C and D, black lines and symbols*). However, the average Syk to Fab' MFI ratios
409 of cNKO B-cells decreased in clusters with Fab' peak FI ≥220 and reduced to levels similar to
410 those in flox control B-cells in clusters with Fab' peak FI ≥240 (*Figure 8C and D, black lines and*
411 *symbols*). These data suggest that increases in the molecular density of BCR clusters, reflected
412 by Fab' peak FI, induce disassociation of Syk from BCR clusters in both flox control and cNKO
413 B-cells. Our results also show that BCR clusters in cNKO B-cells have significantly higher levels
414 of Syk association than in flox control B-cells, even though they have similar Fab' peak
415 intensities.
416
417 We next analyzed the relationship of the pSyk level in individual clusters with BCR molecular
418 density using the method described above. We found that the MFI ratios of pSyk relative to
419 AF546-Fab' gradually decreased with increases in Fab' peak FI in both flox control and cNKO
420 B-cells (*Figure 8E-G, black lines and symbols*), even though we did not observe an increase in
421 pSyk to Fab' MFI ratio at the low Fab' peak FI range. Similar to the Syk to Fab' MFI ratio, the
422 average pSyk to Fab' MFI ratios of individual clusters in cNKO B-cells were much higher than
423 those in flox control B-cells, except for those at the high Fab' peak FI range (*Figure 8E-H*). To
424 confirm this result, we analyzed equal numbers of pSyk clusters in the same cells, based on the
425 criteria of ≥1.3 fold increase in the peak FI compared to the background outside the contact
426 zone with a diameter of ≥250 nm. Similar to clusters identified by AF546-Fab', the average MFI

427 ratios of pSyk to Fab' in these pSyk clusters decreased with increase in their Fab' peak FI in
428 both flox control and cNKO B-cells (*Figure 8I-K, black lines and symbols*). Again, the average
429 pSyk to Fab' MFI ratios of pSyk clusters were much higher in cNKO than flox control B-cells, but
430 were reduced to similar levels in clusters with relatively high Fab' peak FI (*Figure 8K, black line*
431 *and symbols*). Similar reductions of total Syk and pSyk with increasing molecular density of
432 BCR clusters suggest that the disassociation of Syk from BCR clusters, caused by cell
433 contraction-induced increases in molecular density, contributes to BCR signaling attenuation.
434

435 **Increased BCR molecular density by B-cell contraction promotes disassociation of the**
436 **inhibitory phosphatase SHIP-1 from BCR microclusters**

437 The inhibitory phosphatase SHIP-1 is essential for B-cell signaling attenuation (Brauweiler *et al.*
438 2000; Liu *et al.* 2011), suggesting that increases in the molecular density of BCR clusters by B-
439 cell contraction may promote SHIP-1 recruitment. We used the methods described above to
440 address this hypothesis, staining cells for total SHIP-1 (*Figure 9A*) and phosphorylated SHIP-1
441 (pSHIP-1 Y1020) (*Figure 9E*). We found that the average SHIP-1 to Fab' MFI ratios in both flox
442 control and cNKO B-cells decreased with Fab' peak FI at similar rates (*Figure 9A-D, black lines*
443 *and symbols*), even though inhibition of contraction by cNKO reduced the Fab' peak FI of BCR
444 clusters (*Figure 9A-D, brown lines and symbols*). Notably, the reduction in the SHIP-1 to Fab'
445 MFI ratios with increasing Fab' peak FI occurred at the lowest detectable Fab' peak FI (*Figure*
446 *9B-D, brown lines and symbols*), when the Syk to Fab' MFI ratios increased and were sustained
447 (*Figure 8B-D*). Furthermore, this reciprocal relationship between the SHIP-1 to Fab' MFI ratio
448 and Fab' peak FI continued over the entire Fab' peak FI range. It also remained the same in
449 both flox control and cNKO B-cells (*Figure 9B-D*). These results suggest that SHIP-1
450 disassociates from BCR clusters as their molecular density increases, and that the SHIP-1
451 disassociation is more sensitive to the molecular density of BCR clusters than Syk
452 disassociation.

453

454 Similar to the relationship of total SHIP-1 with BCR molecular density, the average MFI ratios of
455 pSHIP-1 relative to AF546-Fab' in individual Fab' clusters decreased with increases in Fab'
456 peak FI at similar rates in flox control and cNKO B-cells (*Figure 9E-H, black lines and symbols*),
457 even though inhibition of contraction by cNKO reduced Fab' peak FI of BCR clusters (*Figure 9E-*
458 *H, brown lines and symbols*). The average pSHIP-1 to Fab' MFI ratios in individual pSHIP-1
459 clusters, detected and analyzed in the same way as pSyk clusters, showed the same decrease
460 with increases in their Fab' peak FI in both flox control and cNKO B-cells (*Figure 9I-K, black*
461 *lines and symbols*). Notably, the average pSHIP-1 to Fab' MFI ratios in individual Fab' or
462 pSHIP-1 clusters in flox control and cNKO B-cells were at similar levels at the same Fab' peak
463 FI ranges (*Figure 9H and K, black lines and symbols*). These results indicate that contraction-
464 induced molecular density increases within individual BCR clusters do not induce preferential
465 recruitment of SHIP-1; instead, it promotes the disassociation of SHIP-1 from BCR clusters.
466

467 **Discussion**

468 When binding membrane-associated antigen, naive follicular B-cells undergo actin-mediated
469 spreading followed by a contraction, which amplifies BCR signaling and promotes
470 immunological synapse formation (Fleire *et al.* 2006; Harwood and Batista 2011). We previously
471 showed that B-cell contraction after spreading on antigen-presenting surfaces promotes BCR
472 signaling attenuation (Liu *et al.* 2013a; Seeley-Fallen *et al.* 2022). However, how the actin
473 cytoskeleton reorganizes as B-cells transition from spreading to contraction and how B-cell
474 contraction downregulates BCR signaling have been elusive. Here, we demonstrate that inner
475 F-actin foci formed at the contact zone distal to the lamellipodial F-actin network promote B-cells
476 to switch from spreading to contraction. These inner foci are derived from the lamellipodial F-
477 actin network that mediates spreading, are generated by N-WASP- but not WASP-activated
478 Arp2/3-mediated branched actin polymerization, and facilitate NMII recruitment. N-WASP-

479 activated actin polymerization coordinates with NMII to form actomyosin ring-like structures,
480 enabling B-cell contraction. B-cell contraction increases BCR molecular density in existing
481 clusters, which promotes the disassociation of both the stimulatory kinase Syk and the inhibitory
482 phosphatase SHIP-1, leading to signaling attenuation.
483
484 One significant finding of this study is that Arp2/3-mediated polymerization of branched actin is
485 required for B-cell contraction. Arp2/3-mediated branched actin polymerization is known to drive
486 B-cell spreading and to create actin centripetal flow at the contact zone between B-cells and
487 antigen-presenting surface (Bolger-Munro *et al.* 2019). The actin structure that supports B- and
488 T-cell spreading to form the immunological synapse with antigen-presenting cells is similar to
489 lamellipodial F-actin networks found in adherent cells (Bunnell *et al.* 2001; Koestler *et al.* 2008;
490 Bolger-Munro *et al.* 2019). Lamellipodial F-actin networks consist primarily of branched actin
491 filaments polymerizing against the plasma membrane interspersed with bundled actin filaments
492 (Krause and Gautreau 2014; Skau and Waterman 2015). Contractile actin structures, such as
493 stress fibers, are typically generated from bundled actin filaments, as observed in adherent and
494 migrating cells (Levayer and Lecuit 2012; Tojkander *et al.* 2015; Hammer *et al.* 2019). Here, we
495 show that inner F-actin foci, generated by Arp2/3-mediated actin polymerization, transition B-
496 cells from spreading to contraction. Furthermore, these inner F-actin foci are directly derived
497 from lamellipodial F-actin networks. Based on the observed dynamics, we infer that instead of
498 polymerizing against the plasma membrane, Arp2/3 appears to nucleate actin polymerization in
499 the opposite direction, sustaining actin foci and their movement away from the lamellipodia. The
500 natural retraction of lamellipodia may contribute to B-cell contraction, but the requirement of
501 inner actin foci argues against it as a primary mechanism for B-cell contraction. This study does
502 not exclude the involvement of bundled actin filaments. Based on the requirement of formin-
503 activated bundled actin filaments for lamellipodial F-actin networks and B-cell spreading (Wang

504 *et al.* 2022), we can speculate that bundled actin filaments may play a role in the formation and
505 movement of these inner F-actin foci, as well as in NMII recruitment.
506
507 Our work provides new insights into distinct functions of the actin nucleation-promoting factors
508 WASP and N-WASP in controlling cell morphology and signaling. Immune cells, including B-
509 cells, express both hematopoietic-specific WASP and the ubiquitous homolog of WASP, N-
510 WASP. These two share high sequence homology, activation mechanism, and Arp2/3 activation
511 function (Padrick and Rosen 2010). We previously identified distinct functions of these two
512 factors unique to B-cells. While both are required for B-cell spreading, N-WASP plays a unique
513 role in B-cell contraction. WASP and N-WASP double knockout B-cells fail to spread on antigen-
514 presenting surfaces, but B-cell-specific N-WASP knockout enhances B-cell spreading and
515 delays B-cell contraction (Liu *et al.* 2013a). WASP and N-WASP appear to have a competitive
516 relationship in B-cells, suppressing each other's activation (Liu *et al.* 2013a). WASP is activated
517 first during B-cell spreading and primarily localized at the periphery of the B-cell contact zone.
518 N-WASP is activated later during B-cell contraction and scattered across the B-cell contact zone
519 (Liu *et al.* 2013a). Here, we reveal the exact role of N-WASP in B-cell contraction – to generate
520 inner F-actin foci from lamellipodial F-actin networks by activating Arp2/3-mediated actin
521 polymerization. N-WASP- but not WASP-activated actin polymerization prolongs the relative
522 lifetime of F-actin foci and facilitates their inward motion toward the center of the contact zone.
523 The delayed activation time and the location in the interior of the contact zone likely give N-
524 WASP a unique opportunity to generate inner F-actin foci. As cNKO only delays and reduces
525 but does not block B-cell contraction and inner F-actin foci formation, other actin factors may be
526 involved, such as the WASP-family verprolin-homologous protein (WAVE) (Rotty *et al.* 2013).
527
528 Our recently published data show that NMII is required for B-cell contraction (Seeley-Fallen *et*
529 *al.* 2022). Activated NMII is recruited to the B-cell contact zone in a SHIP-1-dependent manner.

530 NMII levels reach a plateau at the beginning of B-cell contraction, and NMII forms a peripheral
531 ring surrounding the contact zone during B-cell contraction. Here, we further show that in
532 addition to SHIP-1, N-WASP but not WASP is also involved in NMII recruitment and NMII ring-
533 like structure formation, probably by initiating the generation of inner F-actin foci. Collectively,
534 these findings suggest that SHIP-1 coordinates with N-WASP to recruit NMII. Our previous
535 finding that SHIP-1 promotes B-cell contraction by facilitating N-WASP activation (Liu *et al.*
536 2011; Liu *et al.* 2013a) supports this notion. However, it is surprising that the recruitment of NMII
537 activated by BCR signaling to the contact zone is associated with inhibitory signaling molecules.
538 BCR downstream signaling, including Ca^{2+} fluxes and Rho-family GTPase activation, likely
539 activates NMII motor activity (Vicente-Manzanares *et al.* 2009). The activation switches NMII
540 from the incompetent folded conformation to the competent extended conformation, enabling
541 NMII molecules to bind to F-actin and assemble into contractible bipolar filaments and stacks
542 (Matsumura 2005). A denser F-actin organization has been shown to increase NMII filament
543 stacking (Fenix and Burnette 2018). Here, we showed that the inner F-actin foci generated by
544 N-WASP-activated Arp2/3 are more stable and denser and thus likely promote NMII binding and
545 stacking more efficiently than F-actin generated by WASP-activated Arp2/3. Indeed, our
546 kymograph analysis revealed similar time windows and spatial locations for NMII accumulation
547 and for generating inner F-actin foci from lamellipodial F-actin, supporting our hypothesis. While
548 NMII recruitment is facilitated by inner F-actin foci, the motor activity of NMII is required for the
549 formation of the ring-like structures of inner F-actin foci in return, likely by driving their
550 centripetal movement, thereby providing mechanical feedback for actin reorganization.
551 However, the structural organization of inner F-actin foci and recruited NMII and their
552 coordinated dynamics require further analysis with higher-resolution microscopy techniques.
553
554 Wang et al. (Wang *et al.* 2022) recently showed that B-cells generate actomyosin arcs when
555 interacting with membrane-associated antigen in the presence of adhesion molecules

556 expressed on professional antigen-presenting cells. In contrast to T-cells, B-cells can also
557 respond to membrane-associated antigen without the help of adhesion molecules, when
558 engaging antigen on pathogenic cells, like bacteria, parasites, and cancer cells. While the
559 relationship between actomyosin arcs and inner F-actin foci remains to be explored, the
560 coordinated formation of inner F-actin foci and NMII ring-like structures revealed in our study
561 suggests that these structures are likely the precursors of actomyosin arcs. These structures
562 can potentially be enhanced and matured by adhesion molecule interactions between B-cells
563 and antigen-presenting membranes.
564
565 Our findings suggest an increase in the molecular density within BCR clusters or B-cell
566 synapses as one of the mechanisms by which B-cell contraction promotes BCR signaling
567 attenuation. During contraction, the molecular density of individual BCR clusters, measured by
568 their MFI and peak FI of BCR clustered Fab', increased faster than during the spreading and
569 post-contraction phases. Surprisingly, increases in molecular density induced disassociation of
570 both the stimulatory kinase Syk and the inhibitory phosphatase SHIP-1, contradicting the
571 existing dogma of sequential association of stimulatory and inhibitory signaling molecules with
572 the BCR (Franks and Cambier 2018). Interestingly, the disassociation of SHIP-1 is much more
573 sensitive to BCR molecular density than Syk disassociation. Syk does not disassociate until the
574 molecular density of BCR clusters reaches the top 10% range, while SHIP-1 disassociates from
575 BCR clusters with increases over the entire detectable range of molecular densities. When B-
576 cell contraction is inhibited, the molecular density of BCR clusters is reduced to a range with
577 limited Syk disassociation and normal SHIP-1 disassociation, probably resulting in high Syk to
578 SHIP-1 molecular ratios in BCR clusters than contracting B-cells, increasing BCR signaling
579 levels. The consistency of the data from AF546-Fab' and pSyk or pSHIP-1 clusters supports this
580 notion. However, the resolution of our widefield TIRF imaging limited our ability to examine
581 nascent BCR clusters that actively recruit signaling molecules. Available antibodies did not allow

582 us to simultaneously stain Syk and SHIP-1 or their phosphorylated forms and determine their
583 relative levels in the same cluster. The timing and dynamics of Syk and SHIP-1 recruitment to
584 individual BCR clusters and the direct relationship between Syk and SHIP-1 association and
585 disassociation with BCR clusters and their phosphorylation remain to be further investigated.
586
587 How the molecular density within BCR clusters promotes disassociation of signaling molecules
588 is unknown. We speculate that molecular crowding may displace signaling molecules out of
589 BCR clusters. Supporting this possibility, disassociation of the 145 kDa SHIP-1 is likely to be
590 more sensitive to changes in the molecular density of BCR clusters, compared to disassociation
591 of the 72 kDa Syk. However, these hypotheses need to be further examined. An interesting
592 finding of this study is that the pCD79a and pSyk levels were higher in individual BCR clusters
593 of cNKO B-cells than those of flox control B-cells, even when BCR clusters had similar
594 molecular densities. These data suggest additional mechanisms for B-cell contraction to
595 promote BCR signaling attenuation. In addition to increasing molecular density within BCR
596 clusters, the contractile forces generated by actomyosin rings on the B-cell membrane and BCR
597 clusters may cause changes to the conformations of both BCRs and associated signaling
598 molecules and their lateral interactions in the membrane. These changes may favor the
599 disassociation rather than the association of signaling molecules with BCR clusters. Recently
600 solved molecular assembly structures of both human and mouse BCRs (Dong *et al.* 2022; Su *et*
601 *al.* 2022) support conformational and lateral molecular interaction changes as possible
602 mechanisms for BCR signaling regulation. Similar to the differential impact of the molecular
603 density on the disassociation of Syk and SHIP-1 from BCR clusters, B-cell contraction may
604 differentially affect the interaction of surface BCRs with cytoplasmic and membrane-anchored
605 signaling molecules, such as the lipidated and lipid raft-resident Src kinase Lyn that is
606 responsible for phosphorylating both the immunoreceptor tyrosine-based activation motif (ITAM)

607 of CD79a and the immunoreceptor tyrosine-based inhibitory motif (ITIM) that SHIP-1 binds to
608 (Franks and Cambier 2018).
609
610 Following antigen-induced BCR signaling at immunological synapses, B-cells internalize BCR-
611 captured antigen for processing and presentation. Actomyosin is required for BCR-mediated
612 endocytosis of antigen, particularly surface- and membrane-associated antigen (Natkanski *et al.*
613 2013; Hoogeboom *et al.* 2018; Maeda *et al.* 2021). NMII-mediated traction forces pull BCR-
614 bound antigen off presenting surfaces for endocytosis in an affinity-dependent manner. We
615 have previously shown that when antigens are tightly attached to a surface, high-affinity binding
616 of the BCR to antigens tears the B-cell membrane in an NMII-dependent manner, which triggers
617 lysosome exocytosis and lysosomal enzyme-mediated cleavages of antigen from the associated
618 surface, allowing antigen endocytosis (Maeda *et al.* 2021). While actomyosin plays essential
619 roles in both B-cell contraction and the subsequent antigen endocytosis, whether the
620 actomyosin structure responsible for B-cell contraction also mediates BCR endocytosis remains
621 an interesting and open question. Our early finding that N-WASP is required for BCR
622 endocytosis (Liu *et al.* 2013a) supports this notion. BCR endocytosis can reduce B-cell surface
623 signaling by removing the BCR from the cell surface, transitioning the BCR into an intracellular
624 signaling state (Chaturvedi *et al.* 2008).
625
626 The results presented here have revealed novel insights into the mechanisms underlying actin-
627 facilitated signaling attenuation of the BCR. Taking the previous and current data of our and
628 other labs together, we propose a new working model for such actin-mediated signaling
629 downregulation (*Figure 10*). Upon encountering membrane-associated antigen, such as antigen
630 presented by follicular dendritic cells and on the surfaces of pathogens, mature follicular B-cells
631 undergo rapid spreading, primarily driven by WASP-mediated branched actin polymerization,
632 which maximizes B-cell contact with antigen-presenting surfaces and BCR-antigen

633 engagement, amplifying signaling. Following maximal spreading, N-WASP distal to lamellipodial
634 networks activates Arp2/3-mediated branched actin polymerization, which initiates the formation
635 of inner F-actin foci from lamellipodia towards the center of the B-cell contact zone (*Figure 10*).
636 NMII is then preferentially recruited to these relatively stable inner foci, which promotes the
637 centripetal movement of inner F-actin foci and the maturation of ring-like actomyosin structures,
638 enabling B-cell contraction. B-cell contraction pushes the BCR microclusters formed during B-
639 cell spreading to the center of the contact zone, increasing their molecular density. Increased
640 molecular density promotes the disassociation of signaling molecules from BCR clusters,
641 probably due to crowding and conformational changes, leading to signal downregulation (*Figure*
642 *10*). Inhibitory signaling molecules likely activate the actin reorganization that drives B-cell
643 contraction by promoting the activation and recruitment of NMII to the B-cell contact zone (Liu *et*
644 *al.* 2013a; Seeley-Fallen *et al.* 2022) by hitherto unknown mechanisms. The actomyosin
645 structures responsible for B-cell contraction may further drive B-cells to internalize engaged
646 antigen, further downregulating signaling at the B-cell surface and initiating antigen processing
647 and presentation. Thus, actin reorganization downstream of inhibitory phosphatases reinforces
648 signaling attenuation by driving B-cell contraction.
649

650 **Materials and Methods**

651 Key Reagents Table

Reagent type	Designation	Source	Identifiers	Additional Information
B-cells from C57BL/6 mice	WT	Jackson Laboratories	000664	
B-cells from $WASP^{-/-}$ mice	WKO	Jackson Laboratories	019458	
B-cells from $CD19^{Cre/+}$N-$WASP^{flox/flox}$ mice	cNKO	Lisa Westerberg laboratory		
B-cells from N-$WASP^{flox/flox}$ mice	Flox control	Lisa Westerberg laboratory		

B-cells from LifeAct-GFP mice	LifeAct-GFP	Roberto Weigert laboratory		
B-cells from LifeAct-RFP mice	LifeAct-RFP	Klaus Ley laboratory		
B-cells from GFP-NMIIA mice	GFP-NMIIA	Robert Adelstein laboratory		
Reagent	1,2-dioleoyl-sn-glycero-3-phosphocholine	Avanti Polar Lipids	850375 P	5 mM
Reagent	1,2-dioleoyl-sn-glycero-3-phosphoethanolamine-cap-biotin	Avanti Polar Lipids	870273 C	50 µM
Reagent	Streptavidin	Jackson Immuno Research	016-000-084	1 µg/ml
Antibody	$F(ab')_2$ fragment of goat IgG anti-mouse Ig(G+M) (polyclonal)	Jackson Immuno Research	115-006-068	-
Antibody	Cy3-Fab fragment of goat anti-mouse IgG+M (polyclonal)	Jackson Immuno Research	115-167-020	2.5 µg per 1 x 10^6 cells
Chemical	2-Mercaptoethylamine HCL	Thermo Fisher Scientific	20408	50 mM
Reagent	EZ-Link™ Maleimide-PEG_2-biotin	Thermo Fisher Scientific	A39261	20 mM per mM of protein
Commercial Kit	Alexa Fluor 546 antibody labeling kit	Thermo Fisher Scientific	A20183	-
Ligand	Biotinylated holo-transferrin	Jackson Immuno Research	015-060-050	-
Antibody	Rat IgG_{2b} anti-mouse CD90.2 (Thy1.2) (monoclonal)	Biolegend	105351	1 µl per 2x10^6 cells
Inhibitor	CK-689	Millipore Sigma	182517-25MG	50 µM
Inhibitor	CK-666	Millipore Sigma	SML0006-5MG	50 µM
Inhibitor	Wiskostatin	Millipore Sigma	W2270-5MG	10 µM
Inhibitor	Blebbistatin	Cayman Chemicals	13013	50 µM
Antibody	Rabbit IgG anti-mouse Arp2 antibody (polyclonal)	Abcam	ab47654	1:100
Antibody	Rabbit IgG anti-mouse pWASP antibody (polyclonal)	Thermo Fisher Scientific	PA5-105572	1:100
Antibody	Rabbit IgG anti-mouse pN-WASP antibody (polyclonal)	Thermo Fisher Scientific	PA5-105307	1:100
Antibody	AF488-goat IgG anti-rabbit IgG antibody (polyclonal)	Thermo Fisher Scientific	A-11034	1:200
Antibody	AF546-goat IgG anti-rabbit IgG antibody (polyclonal)	Thermo Fisher Scientific	A-11035	1:200
Reagent	Acti-stain-488 Phalloidin	Cytoskeleton	PHDG1-A	200 nM
Reagent	Acti-stain-555 Phalloidin	Cytoskeleton	PHDH1-A	200 nM

Antibody	Rabbit IgG anti-mouse NMIIA antibody (polyclonal)	Abcam	ab75590	1:100
Antibody	Rabbit IgG anti-mouse pCD79a (Y182) (monoclonal)	Cell Signaling Technology	14732S	1:100
Antibody	Rabbit IgG anti-mouse pSyk (Y519/520) (monoclonal)	Cell Signaling Technology	2710S	1:100
Antibody	Rabbit IgG anti-mouse pSHIP-1 (Y1020) (polyclonal)	Cell Signaling Technology	3941S	1:100
Antibody	Rabbit IgG anti-mouse Syk (polyclonal)	Thermo Fisher Scientific	PA5-17812	1:100
Antibody	Rabbit IgG anti-mouse SHIP-1 (polyclonal)	Thermo Fisher Scientific	PA5-115894	1:100

652

653 **Mice and B-cell isolation**

654 Wild-type (WT) C57BL/6 mice and WASP knockout (WKO) mice on the C57BL/6 background
655 were purchased from Jackson Laboratories. C57BL/6 mice expressing LifeAct-GFP transgene
656 (Riedl *et al.* 2010) were kindly provided by Dr. Roberto Weigert at National Cancer Institute,
657 USA. C57BL/6 mice expressing the LifeAct-RFP transgene were kindly provided by Dr. Klaus
658 Ley at La Jolla Institute for Allergy & Immunology. C57BL/6 mice expressing the GFP-non-
659 muscle myosin IIA (NMIIA) transgene were kindly provided by Dr. Robert Adelstein at the
660 National Heart, Lung, and Blood Institute, USA. WKO mice were bred with LifeAct-GFP mice to
661 obtain LifeAct-GFP-expressing WKO mice. GFP-NMIIA mice were crossed with LifeAct-RFP
662 mice to generate mice expressing both transgenes. N-WASP$^{flox/flox}$ on a 129Sv background
663 (Cotta-de-Almeida *et al.* 2007) were kindly provided by Dr. Lisa Westerberg at Karolinska
664 Institute, Sweden. B-cell-specific N-WASP knockout mice (cNKO, CD19$^{Cre/+}$N-WASP$^{flox/flox}$) and
665 floxed littermate controls (N-WASP$^{flox/flox}$) were obtained by breeding N-WASP$^{flox/flox}$ mice with
666 CD19$^{Cre/+}$ mice on a C57BL/6 background.

667

668 Primary B-cells were isolated from the spleens of 6 to 18 week-old male or female mice, using a
669 previously published protocol (Sharma *et al.* 2009). Briefly, mononuclear cells were isolated by
670 Ficoll density-gradient centrifugation (Millipore Sigma), and T-cells were eliminated by
671 complement-mediated cytolysis with anti-mouse CD90.2 mAb (BD Biosciences) and guinea pig

672 complement (Innovative Research Inc). Monocytes and dendritic cells were eliminated by
673 panning at 37°C and 5% CO_2. Isolated B-cells were kept on ice in DMEM (Lonza) supplemented
674 with 0.6% BSA (Thermo Fisher Scientific). All work involving mice was approved by the
675 Institutional Animal Care and Usage Committee of the University of Maryland.
676
677 **Pseudo-antigen-coated planar lipid bilayers**
678 Planar lipid bilayers (PLB) were prepared using a previously described method (Dustin *et al.*
679 2007; Liu *et al.* 2012a). Briefly, liposomes were generated from a mixture of 5 mM (total
680 concentration) 1,2-dioleoyl-sn-glycero-3-phosphocholine and 1,2-dioleoyl-sn-glycero-3-
681 phosphoethanolamine-cap-biotin (Avanti Polar Lipids) at a 100:1 molar ratio by sonication.
682 Glass coverslips, cleaned overnight with Piranha solution (KMG chemicals), were attached to 8-
683 well chambers (Lab-Tek) and incubated with liposomes (0.05 mM) in PBS for 20 min at room
684 temperature and washed with PBS. The chambers were then incubated with 1 µg/ml
685 streptavidin (Jackson ImmunoResearch Laboratories) for 10 min, washed with PBS, and then
686 incubated with 10 µg/ml mono-biotinylated Fab' fragment of goat anti-mouse Ig(G+M) (pseudo-
687 antigen) (Fab'-PLB) for 10 min, followed by PBS wash. For transferrin-coated PLB (Tf-PLB), 16
688 16 µg/ml biotinylated holoTF was used. To visualize Fab' clustering, a mixture of 0.5 µg/ml
689 Alexa Fluor (AF) 546-labeled and 9.5 µg/ml unlabeled mono-biotinylated Fab' fragment of goat
690 anti-mouse Ig(G+M) was used. The lateral mobility of AF546-Fab' on the PLB was tested using
691 fluorescence recovery after photobleaching (FRAP) to ensure ≥85% AF546 fluorescence
692 recovery within 1 min after photobleaching using a Zeiss LSM 710 equipped with a 60X oil-
693 immersion objective.
694
695 Mono-biotinylated Fab' fragments were generated as previously described (Liu *et al.* 2011).
696 Briefly, the disulfide bond linking the two Fab fragments of $F(ab')_2$ goat anti-mouse Ig(G+M) was
697 reduced using 2-mercaptoethylamine HCL (Thermo Fisher Scientific) and biotinylated by using

698 maleimide-PEG_2-biotin (Thermo Fisher Scientific). Mono-biotinylated Fab' fragments of goat
699 anti-mouse Ig(G+M) were labeled with AF546 using an Alexa Fluor 546 antibody labeling kit
700 (Thermo Fisher Scientific). The molar ratio of AF546 to Fab' in the AF546-labeled Fab' was ~2
701 determined by a Nanodrop spectrophotometer (Nanodrop Technologies).
702
703 **Total internal fluorescence microscopy**
704 To visualize molecules proximal to interacting sites between B-cells and Fab'- or Tf-PLB, we
705 utilized total internal reflection fluorescence microscopy (TIRF) and interference reflection
706 microscopy (IRM). Images were acquired using a Nikon TIRF system on an inverted microscope
707 (Nikon TE2000-PFS, Nikon Instruments Inc.) equipped with a 60X, NA 1.49 Apochromat TIRF
708 objective (Nikon), a Coolsnap HQ2 CCD camera (Roper Scientific), and two solid-state lasers of
709 wavelength 491 and 561 nm. IRM, AF488, and AF546 images were acquired sequentially.
710
711 The plasma membrane area of B-cells contacting PLB was determined using IRM images and
712 custom MATLAB codes. Whether a B-cell contracted or not was determined using the area
713 versus time plots, wherein if a B-cell's contact zone area reduced by ≥5% for at least 10 sec
714 after reaching a maximum value, it was classified as contracting. To image intracellular
715 molecules, B-cells were incubated with Fab'-PLBs for varying lengths of time in PBS at 37°C,
716 fixed with 4% paraformaldehyde, permeabilized with 0.05% saponin, and stained for various
717 molecules. For live-cell imaging, B-cells were pre-warmed to 37°C and imaged as soon as B-
718 cells were dropped into coverslip chambers coated with Fab'-PLB containing PBS in a humidity
719 chamber at 37°C, at 2 sec per frame, up to 7 min. All images from multiple independent
720 experiments were analyzed using NIH ImageJ and custom MatLab scripts. Acquired
721 fluorescence intensity (FI) data were normalized to the one with the lowest FI.
722

723 **Inhibitors**

724 CK-666 (50 μM, Millipore Sigma) was used to perturb Arp2/3 activity (Nolen *et al.* 2009), and its
725 non-functional derivative CK-689 (50 μM, Millipore Sigma) as a control. CK-666 or CK-689 was
726 added at either 0 min, the start of incubation with Fab'-PLB, or at 2 min when most B-cells
727 reached maximum spreading. Notably, B-cells take approximately 1 to 1.5 min to land on PLB.
728 The time when B-cells were added to Fab'-PLB is referred to as 0 min, and the time when B-
729 cells landed on PLB as the start of spreading. The effectiveness of CK-666 was determined by
730 its inhibitory effects on the recruitment of Arp2/3, stained by an anti-Arp2 antibody (Abcam), to
731 the B-cell contact zone using TIRF (*Figure 1-figure supplement 2*). Wiskostatin (Wisko, 10 μM,
732 Millipore Sigma) was used to perturb N-WASP activity in B-cells (Peterson *et al.* 2004), with
733 DMSO used as a vehicle control. Splenic B-cells were pretreated with Wisko for 10 min at 37°C
734 before and during incubation with Fab'-PLB. The effectiveness of Wisko was determined by its
735 inhibitory effects on the level of phosphorylated N-WASP in the B-cell contact zone using
736 immunostaining and TIRF (*Figure 1-figure supplement 4A and C)*. Possible effects of Wisko on
737 WASP activation were evaluated by measuring the mean fluorescence intensity (MFI) of
738 phosphorylated WASP in the contact zone of B-cells treated with or without Wisko for 10 min
739 (*Figure 1-figure supplement 4B and D*). Blebbistatin (Bleb, 50 μM, Cayman Chemicals) was
740 used to inhibit the NMII motor activity (Seeley-Fallen *et al.* 2022). Splenic B-cells were
741 pretreated with Bleb for 20 min before and during incubation with Fab'-PLB.

742

743 **Analysis of the actin cytoskeleton**

744 F-actin was visualized by phalloidin staining in fixed cells and by LifeAct-GFP or LifeAct-RFP
745 expressed by primary B-cells from transgenic mice in live cells. Inner F-actin foci, visualized by
746 both phalloidin staining and LifeAct-GFP, were identified using NIH ImageJ based on the
747 following three criteria: 1) ≥250 nm in diameter, 2) peak fluorescence intensity (FI) ≥2 fold higher
748 than the FI of a nearby area containing no foci, and 3) ≥1 μm away from the outer edge of the B-

749 cell contact zone. The horizontal or vertical length of a focus was measured, and the lesser of
750 the two values was used as its diameter. To analyze the spatiotemporal relationship between
751 inner F-actin foci and the lamellipodial F-actin network, we generated 8 radially and equally
752 spaced kymographs from each cell using time-lapse images and MATLAB. Each kymograph
753 was either classified as contracting or not contracting based on the movement of the leading
754 edge of the B-cell contact zone. The percentage of 8 kymographs from each cell exhibiting inner
755 F-actin foci that could be traced back to lamellipodial F-actin when the B-cell switched from
756 spreading to contraction was determined.
757 The relative speeds and lifetimes of F-actin foci were determined using three kymographs from
758 each B-cell (positioned to track as many inner F-actin foci as possible) and F-actin foci
759 emerging during a 60-sec window right after B-cell maximal spreading. Only those remaining
760 visible in individual kymographs for at least 4 sec were analyzed. The time duration of each F-
761 actin focus detected in a kymograph was used to determine the relative lifetime. The distances
762 individual F-actin foci moved during their lifetimes were used to determine the relative speed.
763 The term 'relative' has been used because the disappearance of an F-actin focus could be due
764 to its movement away from the region used for the kymograph or vertically from the TIRF
765 evanescent field of excitation.
766 To determine the rate of myosin recruitment, GFP-NMIIA MFI in the B-cell contact zone was
767 plotted over time, and the slope for the initial segment of the MFI versus the time plot was
768 determined using linear regression. The percentage of B-cells with the NMIIA ring was
769 determined by visual inspection.
770
771 **Analysis of BCR-Fab' clusters**
772 BCR clusters were identified by clustering of AF546-Fab' on PLBs using custom code by
773 MATLAB. We utilized the median FI of the Fab'-PLB within the same area outside but near the
774 B-cell contact zone as the background. The median, but not mean FI value, was used for

775 background FI calculations to minimize fluctuations due to debris. To ensure that individual
776 clusters with varying FI were detected as distinct objects, we used 16 graded thresholds from
777 1.1 to 4.1 fold of the background (0.2 fold apart) to acquire 16 sets of binary masks for each
778 frame of time-lapse images from each cell. When clusters were detected by multiple thresholds
779 at the same location, only the one identified by the highest threshold was retained. Objects that
780 were smaller than 250 nm in diameter or could not be tracked for at least 20 sec were
781 eliminated. This allowed us to detect the position of BCR-Fab' clusters and track them over time
782 until they merged with other clusters. The horizontal or vertical length of a focus was measured,
783 and the lesser of the two values was used as its diameter. We chose the peak FI as a metric for
784 the extent of Fab' clustering by the BCR, because it does not rely on the area occupied by each
785 cluster. The rate of peak FI increase was determined by linear regression of peak FI versus time
786 curves for each cluster for a given window of time.
787
788 **BCR signaling**
789 Splenic B-cells were incubated with AF546-Fab'-PLB at 37°C and fixed at 1, 3, 5, 7, and 9 min.
790 After fixation, cells were stained for phosphorylated CD79a (pCD79a, Y182) (Cell Signaling
791 Technology), Syk (pSyk, Y519/520) (Cell Signaling Technology), SHIP-1 (pSHIP-1, Y1020) (Cell
792 Signaling Technology), or total Syk or SHIP-1 proteins (Thermo Fisher Scientific). We identified
793 BCR-Fab' clusters as described. We determined the peak FI of AF546-Fab' and the MFI of
794 AF546-Fab', pCD79a, pSyk, pSHIP-1, Syk, or SHIP-1 within each cluster. The ratio of pCD79a
795 MFI to AF546-Fab' MFI in the same cluster was used to estimate the relative phosphorylation
796 level of BCRs in that cluster. This MFI ratio was plotted against AF546-Fab' peak FI to analyze
797 the relationship between BCR phosphorylation and BCR density of individual clusters. We
798 calculated the MFI ratio of Syk to Fab' or SHIP-1 to Fab' in individual clusters to estimate the
799 relative recruitment level of Syk or SHIP-1 to BCR clusters. We plotted these MFI ratios against
800 Fab' peak FI to determine the relationship between Syk and SHIP-1 recruitment levels and BCR

801 density in individual clusters. We calculated the MFI ratio of pSyk to Fab' or pSHIP-1 to Fab' to
802 estimate the amount of pSyk or pSHIP-1 relative to BCR in individual clusters. We plotted these
803 MFI ratios against Fab' peak FI to determine the relationship between Syk or SHIP-1
804 phosphorylation and BCR density in individual clusters. We identified pSyk or pSHIP-1 puncta
805 using the criteria: ≥1.3 fold of the background staining outside the B-cell contact zone and ≥250
806 nm in diameter. We calculated the MFI ratio of pSyk to Fab' or pSHIP-1 to Fab' in individual
807 puncta to estimate the amount of pSyk or pSHIP-1 relative to BCR in individual puncta. We
808 plotted these MFI ratios against Fab' peak FI to determine the relationship between Syk or
809 SHIP-1 phosphorylation and BCR density in individual puncta. We determined the fraction of
810 clusters with graded increases in Fab' peak FI (every 20 FI units) out of the total to analyze the
811 distribution of clusters with different Fab' peak FI. We also determine the average MFI ratios of
812 pCD79a, Syk, pSyk, SHIP-1, and pSHIP-1 relative to Fab' in each graded cluster population.
813 We further divided AF546-Fab' clusters into three populations based on their peak AF546-Fab'
814 FI, relatively low (<190), medium (190-280), and high (>280, detected only in contracted cells)
815 and compared the MFI ratios of pCD79a, pSyk, pSHIP-1, Syk, and SHIP-1 relatively to AF546-
816 Fab' among the three populations using statistical analysis described below. The data were
817 generated from 3 independent experiments with 20~23 (60~69 total) cells and 125~140
818 individual clusters (1500~1680 total) per condition, per time point, and per experiment.
819

820 **Statistical analysis**

821 Statistical analysis was performed using the Mann-Whitney U non-parametric test for unpaired
822 groups having different sample sizes or the Student's *t*-test for paired groups with the same
823 sample size. To compare curves, Kolmogorov-Smirnov test was used. Statistical analyses were
824 performed in Microsoft Excel, GraphPad Prism, and MATLAB. All data are presented as mean ±
825 SEM (standard error of the mean). When testing multiple hypotheses, *p*--values acquired using

826 t-tests were corrected using the Benjamini-Hochberg/Yekutieli method for false discovery rate
827 control.
828
829 **MATLAB scripts**
830 All MATLAB scripts used for this study are available as supplemental materials.
831
832 **Acknowledgements**
833 This work was supported by NIH grants GM064625 (NWA and WS), GM145313 (AU), and
834 AI122205 (AU and WS). We would like to acknowledge Amy Beaven and Kenneth Class for
835 technical support from the Confocal Microcopy and Flow Cytometry cores. We would like to
836 thank Dr. Norma W. Andrews (University of Maryland, College Park) for her careful reading and
837 critical comments on the manuscript.
838
839 **References**
840 Adachi, T., Wienands, J., Wakabayashi, C., Yakura, H., Reth, M. and Tsubata, T. (2001) 'SHP-1
841 requires inhibitory co-receptors to down-modulate B cell antigen receptor-mediated
842 phosphorylation of cellular substrates', *J Biol Chem*, 276(28), 26648-55, available:
843 http://dx.doi.org/10.1074/jbc.M100997200.
844
845 Aman, M.J., Lamkin, T.D., Okada, H., Kurosaki, T. and Ravichandran, K.S. (1998) 'The inositol
846 phosphatase SHIP inhibits Akt/PKB activation in B cells', *J Biol Chem*, 273(51), 33922-8,
847 available: http://dx.doi.org/10.1074/jbc.273.51.33922.
848
849 Batista, F.D. and Harwood, N.E. (2009) 'The who, how and where of antigen presentation to B
850 cells', *Nat Rev Immunol*, 9(1), 15-27, available: http://dx.doi.org/10.1038/nri2454.
851
852 Batista, F.D., Treanor, B. and Harwood, N.E. (2010) 'Visualizing a role for the actin cytoskeleton
853 in the regulation of B-cell activation', *Immunol Rev*, 237(1), 191-204, available:
854 http://dx.doi.org/10.1111/j.1600-065X.2010.00943.x.
855
856 Bolger-Munro, M., Choi, K., Scurll, J.M., Abraham, L., Chappell, R.S., Sheen, D., Dang-Lawson,
857 M., Wu, X., Priatel, J.J., Coombs, D., Hammer, J.A. and Gold, M.R. (2019) 'Arp2/3
858 complex-driven spatial patterning of the BCR enhances immune synapse formation,

BCR signaling and B cell activation', *Elife*, 8, available: http://dx.doi.org/10.7554/eLife.44574.

Bolland, S., Pearse, R.N., Kurosaki, T. and Ravetch, J.V. (1998) 'SHIP modulates immune receptor responses by regulating membrane association of Btk', *Immunity*, 8(4), 509-16, available: http://dx.doi.org/10.1016/s1074-7613(00)80555-5.

Brauweiler, A.M., Tamir, I. and Cambier, J.C. (2000) 'Bilevel control of B-cell activation by the inositol 5-phosphatase SHIP', *Immunol Rev*, 176, 69-74.

Bunnell, S.C., Kapoor, V., Trible, R.P., Zhang, W. and Samelson, L.E. (2001) 'Dynamic actin polymerization drives T cell receptor-induced spreading: a role for the signal transduction adaptor LAT', *Immunity*, 14(3), 315-29, available: http://dx.doi.org/10.1016/s1074-7613(01)00112-1.

Carrasco, Y.R., Fleire, S.J., Cameron, T., Dustin, M.L. and Batista, F.D. (2004) 'LFA-1/ICAM-1 interaction lowers the threshold of B cell activation by facilitating B cell adhesion and synapse formation', *Immunity*, 20(5), 589-99.

Chaturvedi, A., Dorward, D. and Pierce, S.K. (2008) 'The B cell receptor governs the subcellular location of Toll-like receptor 9 leading to hyperresponses to DNA-containing antigens', *Immunity*, 28(6), 799-809, available: http://dx.doi.org/10.1016/j.immuni.2008.03.019.

Cotta-de-Almeida, V., Westerberg, L., Maillard, M.H., Onaldi, D., Wachtel, H., Meelu, P., Chung, U.I., Xavier, R., Alt, F.W. and Snapper, S.B. (2007) 'Wiskott Aldrich syndrome protein (WASP) and N-WASP are critical for T cell development', *Proc Natl Acad Sci U S A*, 104(39), 15424-9, available: http://dx.doi.org/10.1073/pnas.0706881104.

Cyster, J.G. (2010) 'B cell follicles and antigen encounters of the third kind', *Nat Immunol*, 11(11), 989-96, available: http://dx.doi.org/10.1038/ni.1946.

Dal Porto, J.M., Gauld, S.B., Merrell, K.T., Mills, D., Pugh-Bernard, A.E. and Cambier, J. (2004) 'B cell antigen receptor signaling 101', *Mol Immunol*, 41(6-7), 599-613, available: http://dx.doi.org/10.1016/j.molimm.2004.04.008.

Depoil, D., Weber, M., Treanor, B., Fleire, S.J., Carrasco, Y.R., Harwood, N.E. and Batista, F.D. (2009) 'Early events of B cell activation by antigen', *Sci Signal*, 2(63), pt1, available: http://dx.doi.org/10.1126/scisignal.263pt1.

Dong, Y., Pi, X., Bartels-Burgahn, F., Saltukoglu, D., Liang, Z., Yang, J., Alt, F.W., Reth, M. and Wu, H. (2022) 'Structural principles of B cell antigen receptor assembly', *Nature*, 612(7938), 156-161, available: http://dx.doi.org/10.1038/s41586-022-05412-7.

902 Dustin, M.L., Starr, T., Varma, R. and Thomas, V.K. (2007) 'Supported planar bilayers for study
903 of the immunological synapse', *Curr Protoc Immunol*, Chapter 18, Unit 18.13, available:
904 http://dx.doi.org/10.1002/0471142735.im1813s76.

905

906 Fenix, A.M. and Burnette, D.T. (2018) 'Assembly of myosin II filament arrays: Network
907 Contraction versus Expansion', *Cytoskeleton (Hoboken)*, 75(12), 545-549, available:
908 http://dx.doi.org/10.1002/cm.21487.

909

910 Fleire, S.J., Goldman, J.P., Carrasco, Y.R., Weber, M., Bray, D. and Batista, F.D. (2006) 'B cell
911 ligand discrimination through a spreading and contraction response', *Science*,
912 312(5774), 738-41, available: http://dx.doi.org/10.1126/science.1123940.

913

914 Franks, S.E. and Cambier, J.C. (2018) 'Putting on the Brakes: Regulatory Kinases and
915 Phosphatases Maintaining B Cell Anergy', *Front Immunol*, 9, 665, available:
916 http://dx.doi.org/10.3389/fimmu.2018.00665.

917

918 Freeman, S.A., Lei, V., Dang-Lawson, M., Mizuno, K., Roskelley, C.D. and Gold, M.R. (2011)
919 'Cofilin-mediated F-actin severing is regulated by the Rap GTPase and controls the
920 cytoskeletal dynamics that drive lymphocyte spreading and BCR microcluster formation',
921 *J Immunol*, 187(11), 5887-900, available: http://dx.doi.org/10.4049/jimmunol.1102233.

922

923 Gitlin, A.D., Shulman, Z. and Nussenzweig, M.C. (2014) 'Clonal selection in the germinal centre
924 by regulated proliferation and hypermutation', *Nature*, 509(7502), 637-40, available:
925 http://dx.doi.org/10.1038/nature13300.

926

927 Gonzalez, S.F., Pitcher, L.A., Mempel, T., Schuerpf, F. and Carroll, M.C. (2009) 'B cell
928 acquisition of antigen in vivo', *Curr Opin Immunol*, 21(3), 251-7, available:
929 http://dx.doi.org/10.1016/j.coi.2009.05.013.

930

931 Gross, A.J., Lyandres, J.R., Panigrahi, A.K., Prak, E.T. and DeFranco, A.L. (2009)
932 'Developmental acquisition of the Lyn-CD22-SHP-1 inhibitory pathway promotes B cell
933 tolerance', *J Immunol*, 182(9), 5382-92, available:
934 http://dx.doi.org/10.4049/jimmunol.0803941.

935

936 Hammer, J.A., Wang, J.C., Saeed, M. and Pedrosa, A.T. (2019) 'Origin, Organization,
937 Dynamics, and Function of Actin and Actomyosin Networks at the T Cell Immunological
938 Synapse', *Annu Rev Immunol*, 37, 201-224, available: http://dx.doi.org/10.1146/annurev-
939 immunol-042718-041341.

940

941 Harwood, N.E. and Batista, F.D. (2010) 'Early events in B cell activation', *Annu Rev Immunol*,
942 28, 185-210, available: http://dx.doi.org/10.1146/annurev-immunol-030409-101216.

943

944 Harwood, N.E. and Batista, F.D. (2011) 'The cytoskeleton coordinates the early events of B-cell
945 activation', *Cold Spring Harb Perspect Biol*, 3(2), available:
946 http://dx.doi.org/10.1101/cshperspect.a002360.

947

948 Hoogeboom, R., Natkanski, E.M., Nowosad, C.R., Malinova, D., Menon, R.P., Casal, A. and
949 Tolar, P. (2018) 'Myosin IIa Promotes Antibody Responses by Regulating B Cell
950 Activation, Acquisition of Antigen, and Proliferation', *Cell Rep*, 23(8), 2342-2353,
951 available: http://dx.doi.org/10.1016/j.celrep.2018.04.087.

952

953 Hoogeboom, R. and Tolar, P. (2016) 'Molecular Mechanisms of B Cell Antigen Gathering and
954 Endocytosis', *Curr Top Microbiol Immunol*, 393, 45-63, available:
955 http://dx.doi.org/10.1007/82_2015_476.

956

957 Kinnon, C., Hinshelwood, S., Levinsky, R.J. and Lovering, R.C. (1993) 'X-linked
958 agammaglobulinemia--gene cloning and future prospects', *Immunol Today*, 14(11), 554-
959 8, available: http://dx.doi.org/10.1016/0167-5699(93)90187-P.

960

961 Kläsener, K., Maity, P.C., Hobeika, E., Yang, J. and Reth, M. (2014) 'B cell activation involves
962 nanoscale receptor reorganizations and inside-out signaling by Syk', *Elife*, 3, e02069.

963

964 Koestler, S.A., Auinger, S., Vinzenz, M., Rottner, K. and Small, J.V. (2008) 'Differentially
965 oriented populations of actin filaments generated in lamellipodia collaborate in pushing
966 and pausing at the cell front', *Nat Cell Biol*, 10(3), 306-13, available:
967 http://dx.doi.org/10.1038/ncb1692.

968

969 Krause, M. and Gautreau, A. (2014) 'Steering cell migration: lamellipodium dynamics and the
970 regulation of directional persistence', *Nat Rev Mol Cell Biol*, 15(9), 577-90, available:
971 http://dx.doi.org/10.1038/nrm3861.

972

973 Kurosaki, T. (2000) 'Functional dissection of BCR signaling pathways', *Curr Opin Immunol*,
974 12(3), 276-81.

975

976 Kurosaki, T., Shinohara, H. and Baba, Y. (2010) 'B cell signaling and fate decision', *Annu Rev*
977 *Immunol*, 28, 21-55, available:
978 http://dx.doi.org/10.1146/annurev.immunol.021908.132541.

979

980 Kwak, K., Akkaya, M. and Pierce, S.K. (2019) 'B cell signaling in context', *Nat Immunol*, 20(8),
981 963-969, available: http://dx.doi.org/10.1038/s41590-019-0427-9.

982

983 Leung, W.H., Tarasenko, T., Biesova, Z., Kole, H., Walsh, E.R. and Bolland, S. (2013) 'Aberrant
984 antibody affinity selection in SHIP-deficient B cells', *Eur J Immunol*, 43(2), 371-81,
985 available: http://dx.doi.org/10.1002/eji.201242809.

986

987 Levayer, R. and Lecuit, T. (2012) 'Biomechanical regulation of contractility: spatial control and
988 dynamics', *Trends Cell Biol*, 22(2), 61-81, available:
989 http://dx.doi.org/10.1016/j.tcb.2011.10.001.

990

991 Liu, C., Bai, X., Wu, J., Sharma, S., Upadhyaya, A., Dahlberg, C.I., Westerberg, L.S., Snapper,
992 S.B., Zhao, X. and Song, W. (2013a) 'N-WASP is essential for the negative regulation of
993 B cell receptor signaling', *PLoS Biol*, 11(11), e1001704, available:
994 http://dx.doi.org/10.1371/journal.pbio.1001704.

995

996 Liu, C., Fallen, M.K., Miller, H., Upadhyaya, A. and Song, W. (2013b) 'The actin cytoskeleton
997 coordinates the signal transduction and antigen processing functions of the B cell
998 antigen receptor', *Front Biol (Beijing)*, 8(5), 475-485, available:
999 http://dx.doi.org/10.1007/s11515-013-1272-0.

1000

1001 Liu, C., Miller, H., Hui, K.L., Grooman, B., Bolland, S., Upadhyaya, A. and Song, W. (2011) 'A
1002 balance of Bruton's tyrosine kinase and SHIP activation regulates B cell receptor cluster
1003 formation by controlling actin remodeling', *J Immunol*, 187(1), 230-9, available:
1004 http://dx.doi.org/10.4049/jimmunol.1100157.

1005

1006 Liu, C., Miller, H., Orlowski, G., Hang, H., Upadhyaya, A. and Song, W. (2012a) 'Actin
1007 reorganization is required for the formation of polarized B cell receptor signalosomes in
1008 response to both soluble and membrane-associated antigens', *J Immunol*, 188(7), 3237-
1009 46, available: http://dx.doi.org/10.4049/jimmunol.1103065.

1010

1011 Liu, C., Miller, H., Sharma, S., Beaven, A., Upadhyaya, A. and Song, W. (2012b) 'Analyzing
1012 actin dynamics during the activation of the B cell receptor in live B cells', *Biochem*
1013 *Biophys Res Commun*, 427(1), 202-6, available:
1014 http://dx.doi.org/10.1016/j.bbrc.2012.09.046.

1015

1016 Maeda, F.Y., van Haaren, J.J., Langley, D.B., Christ, D., Andrews, N.W. and Song, W. (2021)
1017 'Surface-associated antigen induces permeabilization of primary mouse B-cells and
1018 lysosome exocytosis facilitating antigen uptake and presentation to T-cells', *Elife*, 10,
1019 available: http://dx.doi.org/10.7554/eLife.66984.

1020

1021 Matsumura, F. (2005) 'Regulation of myosin II during cytokinesis in higher eukaryotes', *Trends*
1022 *Cell Biol*, 15(7), 371-7, available: http://dx.doi.org/10.1016/j.tcb.2005.05.004.

1023

1024 Mizuno, K., Tagawa, Y., Mitomo, K., Arimura, Y., Hatano, N., Katagiri, T., Ogimoto, M. and
1025 Yakura, H. (2000) 'Src homology region 2 (SH2) domain-containing phosphatase-1
1026 dephosphorylates B cell linker protein/SH2 domain leukocyte protein of 65 kDa and
1027 selectively regulates c-Jun NH2-terminal kinase activation in B cells', *J Immunol*, 165(3),
1028 1344-51, available: http://dx.doi.org/10.4049/jimmunol.165.3.1344.

1029

1030 Natkanski, E., Lee, W.Y., Mistry, B., Casal, A., Molloy, J.E. and Tolar, P. (2013) 'B cells use
1031 mechanical energy to discriminate antigen affinities', *Science*, 340(6140), 1587-90,
1032 available: http://dx.doi.org/10.1126/science.1237572.

1033
1034 Nolen, B.J., Tomasevic, N., Russell, A., Pierce, D.W., Jia, Z., McCormick, C.D., Hartman, J.,
1035 Sakowicz, R. and Pollard, T.D. (2009) 'Characterization of two classes of small molecule
1036 inhibitors of Arp2/3 complex', *Nature*, 460(7258), 1031-4, available:
1037 http://dx.doi.org/10.1038/nature08231.

1038
1039 Padrick, S.B. and Rosen, M.K. (2010) 'Physical mechanisms of signal integration by WASP
1040 family proteins', *Annu Rev Biochem*, 79, 707-35, available:
1041 http://dx.doi.org/10.1146/annurev.biochem.77.060407.135452.

1042
1043 Pao, L.I., Lam, K.P., Henderson, J.M., Kutok, J.L., Alimzhanov, M., Nitschke, L., Thomas, M.L.,
1044 Neel, B.G. and Rajewsky, K. (2007) 'B cell-specific deletion of protein-tyrosine
1045 phosphatase Shp1 promotes B-1a cell development and causes systemic autoimmunity',
1046 *Immunity*, 27(1), 35-48, available: http://dx.doi.org/10.1016/j.immuni.2007.04.016.

1047
1048 Peterson, J.R., Bickford, L.C., Morgan, D., Kim, A.S., Ouerfelli, O., Kirschner, M.W. and Rosen,
1049 M.K. (2004) 'Chemical inhibition of N-WASP by stabilization of a native autoinhibited
1050 conformation', *Nat Struct Mol Biol*, 11(8), 747-55, available:
1051 http://dx.doi.org/10.1038/nsmb796.

1052
1053 Pierce, S.K. (2002) 'Lipid rafts and B-cell activation', *Nat Rev Immunol*, 2(2), 96-105, available:
1054 http://dx.doi.org/10.1038/nri726.

1055
1056 Reth, M. (1994) 'B cell antigen receptors', *Curr Opin Immunol*, 6(1), 3-8.

1057
1058 Reth, M. and Wienands, J. (1997) 'Initiation and processing of signals from the B cell antigen
1059 receptor', *Annu Rev Immunol*, 15, 453-79, available:
1060 http://dx.doi.org/10.1146/annurev.immunol.15.1.453.

1061
1062 Rey-Suarez, I., Wheatley, B.A., Koo, P., Bhanja, A., Shu, Z., Mochrie, S., Song, W., Shroff, H.
1063 and Upadhyaya, A. (2020) 'WASP family proteins regulate the mobility of the B cell
1064 receptor during signaling activation', *Nat Commun*, 11(1), 439, available:
1065 http://dx.doi.org/10.1038/s41467-020-14335-8.

1066
1067 Riedl, J., Flynn, K.C., Raducanu, A., Gärtner, F., Beck, G., Bösl, M., Bradke, F., Massberg, S.,
1068 Aszodi, A., Sixt, M. and Wedlich-Söldner, R. (2010) 'Lifeact mice for studying F-actin
1069 dynamics', *Nat Methods*, 7(3), 168-9, available: http://dx.doi.org/10.1038/nmeth0310-
1070 168.

1071

1072 Rotty, J.D., Wu, C. and Bear, J.E. (2013) 'New insights into the regulation and cellular functions
1073 of the ARP2/3 complex', *Nat Rev Mol Cell Biol*, 14(1), 7-12, available:
1074 http://dx.doi.org/10.1038/nrm3492.

1075

1076 Schreiner, G.F. and Unanue, E.R. (1977) 'Capping and the lymphocyte: models for membrane
1077 reorganization', *J Immunol*, 119(5), 1549-51.

1078

1079 Seeley-Fallen, M.K., Lazzaro, M., Liu, C., Li, Q.Z., Upadhyaya, A. and Song, W. (2022) 'Non-
1080 Muscle Myosin II Is Essential for the Negative Regulation of B-Cell Receptor Signaling
1081 and B-Cell Activation', *Front Immunol*, 13, 842605, available:
1082 http://dx.doi.org/10.3389/fimmu.2022.842605.

1083

1084 Seeley-Fallen, M.K., Liu, L.J., Shapiro, M.R., Onabajo, O.O., Palaniyandi, S., Zhu, X., Tan, T.H.,
1085 Upadhyaya, A. and Song, W. (2014) 'Actin-binding protein 1 links B-cell antigen
1086 receptors to negative signaling pathways', *Proc Natl Acad Sci U S A*, 111(27), 9881-6,
1087 available: http://dx.doi.org/10.1073/pnas.1321971111.

1088

1089 Sharma, S., Orlowski, G. and Song, W. (2009) 'Btk regulates B cell receptor-mediated antigen
1090 processing and presentation by controlling actin cytoskeleton dynamics in B cells', *J*
1091 *Immunol*, 182(1), 329-39.

1092

1093 Shen, Z., Liu, S., Li, X., Wan, Z., Mao, Y., Chen, C. and Liu, W. (2019) 'Conformational change
1094 within the extracellular domain of B cell receptor in B cell activation upon antigen
1095 binding', *Elife*, 8, available: http://dx.doi.org/10.7554/eLife.42271.

1096

1097 Shlomchik, M.J., Luo, W. and Weisel, F. (2019) 'Linking signaling and selection in the germinal
1098 center', *Immunol Rev*, 288(1), 49-63, available: http://dx.doi.org/10.1111/imr.12744.

1099

1100 Skau, C.T. and Waterman, C.M. (2015) 'Specification of Architecture and Function of Actin
1101 Structures by Actin Nucleation Factors', *Annu Rev Biophys*, 44, 285-310, available:
1102 http://dx.doi.org/10.1146/annurev-biophys-060414-034308.

1103

1104 Sohn, H.W., Tolar, P. and Pierce, S.K. (2008) 'Membrane heterogeneities in the formation of B
1105 cell receptor-Lyn kinase microclusters and the immune synapse', *J Cell Biol*, 182(2),
1106 367-79, available: http://dx.doi.org/10.1083/jcb.200802007.

1107

1108 Song, W., Cho, H., Cheng, P. and Pierce, S.K. (1995) 'Entry of B cell antigen receptor and
1109 antigen into class II peptide-loading compartment is independent of receptor cross-
1110 linking', *J Immunol*, 155(9), 4255-63.

1111

1112 Song, W., Liu, C., Seeley-Fallen, M.K., Miller, H., Ketchum, C. and Upadhyaya, A. (2013) 'Actin-
1113 mediated feedback loops in B-cell receptor signaling', *Immunol Rev*, 256(1), 177-89,
1114 available: http://dx.doi.org/10.1111/imr.12113.

1115

1116 Su, Q., Chen, M., Shi, Y., Zhang, X., Huang, G., Huang, B., Liu, D. and Liu, Z. (2022) 'Cryo-EM
1117 structure of the human IgM B cell receptor', *Science*, 377(6608), 875-880, available:
1118 http://dx.doi.org/10.1126/science.abo3923.

1119
1120 Tanaka, S. and Baba, Y. (2020) 'B Cell Receptor Signaling', *Adv Exp Med Biol*, 1254, 23-36,
1121 available: http://dx.doi.org/10.1007/978-981-15-3532-1_2.

1122
1123 Tojkander, S., Gateva, G., Husain, A., Krishnan, R. and Lappalainen, P. (2015) 'Generation of
1124 contractile actomyosin bundles depends on mechanosensitive actin filament assembly
1125 and disassembly', *Elife*, 4, e06126, available: http://dx.doi.org/10.7554/eLife.06126.

1126
1127 Tolar, P., Hanna, J., Krueger, P.D. and Pierce, S.K. (2009a) 'The constant region of the
1128 membrane immunoglobulin mediates B cell-receptor clustering and signaling in
1129 response to membrane antigens', *Immunity*, 30(1), 44-55, available:
1130 http://dx.doi.org/10.1016/j.immuni.2008.11.007.

1131
1132 Tolar, P., Sohn, H.W., Liu, W. and Pierce, S.K. (2009b) 'The molecular assembly and
1133 organization of signaling active B-cell receptor oligomers', *Immunol Rev*, 232(1), 34-41,
1134 available: http://dx.doi.org/10.1111/j.1600-065X.2009.00833.x.

1135
1136 Tolar, P., Sohn, H.W. and Pierce, S.K. (2005) 'The initiation of antigen-induced B cell antigen
1137 receptor signaling viewed in living cells by fluorescence resonance energy transfer', *Nat*
1138 *Immunol*, 6(11), 1168-76, available: http://dx.doi.org/10.1038/ni1262.

1139
1140 Treanor, B., Depoil, D., Gonzalez-Granja, A., Barral, P., Weber, M., Dushek, O., Bruckbauer, A.
1141 and Batista, F.D. (2010) 'The membrane skeleton controls diffusion dynamics and
1142 signaling through the B cell receptor', *Immunity*, 32(2), 187-99, available:
1143 http://dx.doi.org/10.1016/j.immuni.2009.12.005.

1144
1145 Unanue, E.R. and Karnovsky, M.J. (1973) 'Redistribution and fate of Ig complexes on surface of
1146 B lymphocytes: functional implications and mechanisms', *Transplant Rev*, 14, 184-210,
1147 available: http://dx.doi.org/10.1111/j.1600-065x.1973.tb00107.x.

1148
1149 Vicente-Manzanares, M., Ma, X., Adelstein, R.S. and Horwitz, A.R. (2009) 'Non-muscle myosin
1150 II takes centre stage in cell adhesion and migration', *Nat Rev Mol Cell Biol*, 10(11), 778-
1151 90, available: http://dx.doi.org/10.1038/nrm2786.

1152
1153 Wang, H., Morse, H.C. and Bolland, S. (2020) 'Transcriptional Control of Mature B Cell Fates',
1154 *Trends Immunol*, 41(7), 601-613, available: http://dx.doi.org/10.1016/j.it.2020.04.011.

1155
1156 Wang, J.C., Yim, Y.I., Wu, X., Jaumouille, V., Cameron, A., Waterman, C.M., Kehrl, J.H. and
1157 Hammer, J.A. (2022) 'A B-cell actomyosin arc network couples integrin co-stimulation to
1158 mechanical force-dependent immune synapse formation', *Elife*, 11, available:
1159 http://dx.doi.org/10.7554/eLife.72805.

1160
1161 Westerberg, L.S., Dahlberg, C., Baptista, M., Moran, C.J., Detre, C., Keszei, M., Eston, M.A.,
1162 Alt, F.W., Terhorst, C., Notarangelo, L.D. and Snapper, S.B. (2012) 'Wiskott-Aldrich
1163 syndrome protein (WASP) and N-WASP are critical for peripheral B-cell development
1164 and function', *Blood*, 119(17), 3966-74, available: http://dx.doi.org/10.1182/blood-2010-
1165 09-308197.

1166
1167 Yang, J. and Reth, M. (2010) 'Oligomeric organization of the B-cell antigen receptor on resting
1168 cells', *Nature*, 467(7314), 465-9, available: http://dx.doi.org/10.1038/nature09357.

1169

1170 **Figure legend**

1171 **Figure 1. Arp2/3, activated by N-WASP but not WASP, is required for B-cell contraction.**
1172 Splenic B-cells were incubated with planar lipid bilayers coated with monobiotinylated Fab'
1173 fragment of goat anti-mouse IgG+M (Fab'-PLB) in the absence and presence of various
1174 inhibitors and imaged live at 37°C by interference reflection microscopy (IRM). The B-cell
1175 plasma membrane area contacting Fab'-PLB (B-cell contact zone) was measured using IRM
1176 images and custom MATLAB scripts. (**A**) Representative IRM images of splenic B-cells from
1177 C57BL/6 mice treated with CK-689 or CK-666 (50 μM) before (0 min) and after maximal
1178 spreading (2 min). (**B**) Representative plots of the B-cell contact area versus time from one
1179 contracting cell and one non-contracting cell. (**C**) Percentages (±SEM) of B-cells that underwent
1180 contraction after treatment with CK-666 or CK-689. A B-cell was classified as contracting if its
1181 contact zone area was reduced by ≥5% for at least 10 sec after reaching a maximum value. (**D**)
1182 Representative IRM images of splenic B-cells from C57BL/6 mice treated with DMSO or
1183 Wiskostatin (Wisko, 10 μM) 10 min before and during incubation with Fab'-PLB. (**E**)
1184 Percentages (±SEM) of B-cells that underwent contraction after treatment with Wisko or DMSO.
1185 (**F**) Representative IRM images of splenic B-cells from flox control and B-cell-specific N-WASP
1186 knockout (cNKO) mice. (**G**) Percentages (±SEM) of cNKO or flox control B-cells that underwent
1187 contraction. (**H**) Representative IRM images of splenic B-cells from WT or WASP knockout mice
1188 (WKO). (**I**) Percentages (±SEM) of WKO or WT B-cells that underwent contraction. Data points
1189 in **C**, **E**, **G**, and **I** represent three independent experiments, ~25 cells per condition per
1190 experiment, with each color representing one experiment. Scale bar, 2 μm. *p <0.05,
1191 ***p<0.001, by paired student's t-test.

1192 **Figure supplement 1.** B-cells spread and contract on Fab'-coated-planar lipid bilayers.

1193 **Figure supplement 2.** CK-666 significantly decreases Arp2/3 recruitment to the B-cell contact
1194 zone.

1195 **Figure supplement 3.** CK-666 treatment before but not after maximal B-cell spreading
1196 decreases the spreading kinetics.
1197 **Figure supplement 4.** Wiskostatin treatment inhibits N-WASP activation while enhancing
1198 WASP activation in B-cells.
1199 **Figure 1–Video 1.** Effects of CK-666, Wiskostatin, conditional N-WASP knockout, and WASP
1200 knockout on B-cell contraction.
1201
1202 **Figure 2. Arp2/3, downstream of N-WASP, generates inner F-actin foci, driving B-cell**
1203 **contraction.** (**A-C**) WT splenic B-cells were treated with CK-689 or CK-666 (50 μM) during
1204 incubation with Fab'-PLB (**A and B**), and flox control and cNKO B-cells were incubated with
1205 Fab'-PLB at 37ºC **(C)**. Cells were fixed at 2 and 4 min, permeabilized, stained for F-actin with
1206 phalloidin, and analyzed using TIRF. Shown are representative TIRF images of phalloidin
1207 staining in the contact zone of CK-689 and CK-666-treated B-cells (**A,** left panels) and
1208 fluorescence intensity (FI) profiles of phalloidin staining along a line crossing cells (**A,** right
1209 panels). Green arrows indicate lamellipodial F-actin, purple arrows indicate inner F-actin foci on
1210 the line, and blue arrows indicate all inner actin foci forming a ring-like structure. Percentages of
1211 cells (per image) (±SEM) with inner F-actin foci forming ring-like distribution among CK-689-
1212 versus CK-666-treated cells (**B**) and flox control versus cNKO B-cells (**C**) before (2 min) and
1213 after (4 min) contraction were determined by visual inspection of phalloidin FI line-profiles
1214 across the B-cell contact zones. Data points in **B** and **C** represent 3 independent experiments,
1215 with each color representing one experiment, 5 images per condition per experiment, and ~15
1216 cells per image. (**D-G**) Inner F-actin foci were identified by their diameter (≥250 nm), peak FI (≥2
1217 fold of no foci area, and location (1 μm away from the outer edge) and quantified as the number
1218 per cell using TIRF images. (**D**) Shown are representative images of splenic B-cells from
1219 LifeAct-GFP-expressing mice treated with CK-689 or CK-666 from 0 min during incubation with
1220 Fab'-PLB at 37ºC (top) and the average number (±SEM) of inner LifeAct-GFP foci per cell

1221 (bottom) at 2 min. (**E**) LifeAct-GFP B-cells were treated with CK-666 at 2 min. Shown are
1222 representative TIRF images of LifeAct-GFP in the contact zone of B-cells (top) and the average
1223 number (±SEM) of inner LifeAct-GFP foci (bottom) in the same cell 10s before and 20s after
1224 CK-666 treatment. Arrows indicate disappeared actin foci after CK666 treatment. (**F**) Shown are
1225 representative TIRF images of phalloidin-staining in the contact zone of flox control and cNKO
1226 B-cells after incubating with Fab'-PLB for 2 min (top) and the average number (±SEM) of inner
1227 F-actin foci per cell (bottom). (**G**) Shown are representative TIRF images of WT and WKO B-
1228 cells expressing LifeAct-GFP incubated with Fab'-PLB for 2 min and the average number
1229 (±SEM) of inner F-actin foci per cell (bottom). Data points represent individual cells from three
1230 independent experiments with 10 (**D, F, and G**) or 6 (**E**) cells per condition per experiment.
1231 Scale bar, 2 μm. ** p <0.01, *** p<0.001, by non-parametric student's t-test.
1232 **Figure 2-Video 1.** Effects of CK-666 and WKO on F-actin foci formation.
1233
1234 **Figure 3. Inner F-actin foci are originated from lamellipodia behind the spreading**
1235 **membrane.** Mouse splenic B-cells from LifeAct-GFP transgenic mice were treated with DMSO
1236 or Wisko (10 μM), imaged live using TIRF during incubation with Fab'-PLB at 37°C, and
1237 analyzed using kymographs generated by NIH ImageJ. (**A**) One frame of TIRF time-lapse
1238 images of LifeAct-GFP in the contact zone of B-cells treated with DMSO or Wisko and a WKO
1239 B-cell. Lines indicate eight kymographs that were randomly generated from each cell. (**B**)
1240 Representative kymographs were generated from TIRF time-lapse images of LifeAct-GFP at the
1241 red line in (A). Top panel, a contracting cell. Arrows indicate the start of contraction with inner F-
1242 actin foci originating from lamellipodia. Bottom panel, a non-contracting cell. Lamellipodia-
1243 derived inner F-actin foci were identified by their LifeAct-GFP FI ≥2 fold of their nearby region,
1244 migrating out of the lamellipodial F-actin toward the center of the contact zone, and trackable for
1245 >8 sec. (**C**) Percentages (±SEM) of kymographs showing inner F-actin foci originating from
1246 lamellipodia per cell that did and did not undergo contraction. Data were generated from 3

1247 independent experiments with ~10 cells per condition per experiment**.** (**D**) A histogram of inner
1248 F-actin foci emerging (expressed as percentages of the total events, blue line) over time relative
1249 to the time of B-cell contraction (defined as 0 sec, indicated by a purple dash line and arrow).
1250 Data were generated from 5 independent experiments with ~9 cells per condition per
1251 experiment**.** (**E**) Percentage (±SEM) of inner F-actin foci originated from lamellipodia observed
1252 in 8 randomly positioned kymographs of each DMSO- or Wisko-treated WT or untreated WKO
1253 B-cell. Data were generated from 3 independent experiments with ~10 cells per condition per
1254 experiment**.** Scale bars, 2 μm. *** $p<0.001$, by non-parametric student's *t*-test.
1255 **Figure supplement 1.** Emerging of Inner F-actin foci from lamellipodia.
1256
1257 **Figure 4. N-WASP-activated Arp2/3 sustains the lifetime and the centripetal movement of**
1258 **inner F-actin foci.** LifeAct-GFP-expressing B-cells were incubated with or without various
1259 inhibitors and imaged live by TIRF during interaction with Fab'-PLB at 37ºC. Three kymographs
1260 were generated for each cell using time-lapse images and positioned to track as many inner
1261 actin foci as possible. (**A**) A representative kymograph from TIRF time-lapse images of a
1262 DMSO-treated B-cell (Left panels). Inner F-actin foci were identified as described in Figure 3,
1263 and those that emerged during the 60 sec window after maximal spreading (white rectangles in
1264 B) and can be tracked for ≥ 4 sec (dashed lines) in individual kymographs were analyzed.
1265 Relative lifetimes of inner F-actin foci were measured using the duration each focus could be
1266 detected in a kymograph. The relative distances traveled by the foci were measured using the
1267 displacement of each focus in a kymograph. Relative speed was calculated for each inner F-
1268 actin focus by dividing its relative distance by its relative lifetime (right panels). (**B-D**) B-cells
1269 were treated with CK-689 or CK-666 (50 μM) from the beginning of the incubation with Fab'-PLB
1270 (0 min). Shown are representative kymographs (**B**), relative lifetimes (**C**), and relative speed (**D**)
1271 of inner F-actin foci in CK-689- versus CK-666-treated B-cells. (**E-G**) B-cells were treated with
1272 CK-666 at maximal spreading (2 min). Shown are a representative kymograph of a CK-666-

1273 treated cell (**E**), relative lifetimes (**F**), and relative speeds (**G**) of inner F-actin foci in 30-sec
1274 windows before the inhibition and 10 sec after the inhibition in the same cells (linked by blue
1275 lines). (**H-J**) B-cells were treated with DMSO or Wisko (10 μM) 10 min before and during
1276 interaction with Fab'-PLB. Shown is a representative kymograph of a Wisko-treated B-cell **(H)**,
1277 relative lifetime **(I)**, and relative speed **(J)** of inner F-actin foci in DMSO versus Wisko-treated B-
1278 cells. (**K-M**) LifeAct-GFP-expressing WT and WKO B-cells were incubated with Fab'-PLB.
1279 Shown are a representative kymograph of a WKO B-cell (**K**), relative lifetime (**L**), and relative
1280 speed (**M**) of WT versus WKO B-cells. Data points represent the averaged values from inner F-
1281 actin foci in individual cells, with 3 kymographs per cell and ~12 cells per condition per
1282 experiment from 3 independent experiments. Scale bar, 2 μm. * p <0.05, ** p <0.01, ***
1283 p<0.001, by non-parametric and paired student's t-test.
1284
1285 **Figure 5. N-WASP facilitates NMII recruitment and ring-like structure formation, and NMII**
1286 **promotes inner F-actin foci ring maturation.** (**A-C**) B-cells from mice expressing the GFP
1287 fusion of non-muscle myosin IIA (GFP-NMIIA) transgene were treated with DMSO or Wisko (10
1288 μM) 10 min before and during incubation with Fab'-PLB. The B-cell contact zones were imaged
1289 live using TIRF. Shown are representative TIRF images of DMSO- and Wisko-treated B-cells at
1290 30 sec (during spreading) and 2 min 30 sec (after maximal spreading) post landing (**A,** Scale
1291 bars, 2 μm), the averaged GFP-NMIIA MFI (±SEM) (**B**), and the initial rates of increasing
1292 (±SEM) of GFP-NMIIA in the contact zone (the slope of the initial GFP-NMIIA MFI versus time
1293 curves of individual cells) (**C**). Data points represent individual cells from 3 independent
1294 experiments with ~6 cells per condition per experiment. * p <0.05, ***p<0.001, by Kolmogorov-
1295 Smirnov test (**B**) or non-parametric student's t-test (**C**). (**D**) Primary B-cells from mice
1296 expressing both GFP-NMIIA and LifeAct-RFP transgenes were incubated with Fab'-PLB at 37°C
1297 and imaged live by TIRF. Shown are a representative TIRF image of a cell and a kymograph
1298 generated from time-lapse TIRF images at the yellow line. The purple arrow indicates the

1299 starting point of contraction, the white arrow GFP-NMIIA recruitment proximal to the spreading
1300 membrane, and the yellow arrow an F-actin (LifeAct-RFP) focus originating at the lamellipodia
1301 and moving away from the spreading membrane. (**E, F**) Primary B-cells from flox control, WKO,
1302 and cNKO mice were incubated with Fab'-PLB for indicated times. Cells were fixed,
1303 permeabilized, stained for NMII light chain, and imaged by IRM and TIRF. Shown are
1304 representative IRM and TIRF images (**E**) and percentages (±SD) of B-cells with the NMII ring-
1305 like structure in individual images (**F**), identified by visual inspection. The data were generated
1306 from 3 independent experiments with 5 images per condition per experiment. Scale bars, 2 μm.
1307 * p <0.05, ** p <0.01, *** p<0.001, by non-parametric student's t-test. (**G**, **H**) WT splenic B-cells
1308 were treated with DMSO or Blebbistatin (Bleb, 50 μM) 20 min before and during incubation with
1309 Fab'-PLB at 37°C. Cells were fixed at 2 and 4 min, permeabilized, stained with phalloidin, and
1310 imaged by TIRF. Shown are representative TIRF images of the B-cell contact zone (**G**) and
1311 percentages of cells (±SEM) with inner F-actin foci forming ring-like distribution (**H**), determined
1312 as described in Figure 2. Data were generated from 3 independent experiments with ~50 cells
1313 per condition per experiment with different color dots representing individual experiments. Scale
1314 bar, 2 μm. * p <0.05, ** p<0.01 by paired student's t-test.
1315 **Figure 5-Video 1.** Wiskostatin treatment inhibits NMII ring-like structure formation.
1316
1317 **Figure 6. B-cell contraction increases the molecular density within BCR clusters.** Primary
1318 B-cells from WT mice were treated with CK-689 or CK-666 from the beginning of the incubation
1319 with AF546-Fab'-PLB (0 min) or at the maximal B-cell spreading (2 min) (**A, D, E, H, I, N, O**).
1320 WT B-cells were treated with DMSO or Wisko (10 μM) 10 min before and during the incubation
1321 with AF546-Fab'-PLB (**B, F, J, P**). B-cells from flox control and cNKO mice were incubated with
1322 AF546-Fab'-PLB (**C, G, K, Q**). The B-cell contact zones were imaged live by TIRF. (**A-C**)
1323 Representative time-lapse images at 30 sec (during B-cell spreading) and 2 min 30 sec (after
1324 maximal spreading) after cell landed. Scale bars, 2 μm. (**D-G**) The MFI of AF546-Fab' in the

1325 contact zone was plotted over time. Purple rectangles indicate the contraction phase based on
1326 the changes in the average B-cell contact area over time. (**H-K**) Rates of AF546-Fab' MFI
1327 increases in the B-cell contact zone before and during contraction were determined by the slope
1328 of AF546-Fab' MFI versus time plots. Data points represent individual cells and were generated
1329 from 3 independent experiments with 6-12 cells per experiment. * p <0.05, ** p <0.01, ***
1330 p<0.001, by Kolmogorov-Smirnov test (D-G) or paired student's t-test (H-K). (**L**) A
1331 representative frame from a time-lapse of a CK-689-treated B-cell (left) shows AF546-Fab'
1332 clusters 30 sec after contraction began, and enlarged time-lapse images (right) show a single
1333 AF546-Fab' cluster over a 40-sec time window after contraction began. AF546 clusters were
1334 identified using the criteria: ≥250 nm in diameter, ≥1.1 fold of FI outside the B-cell contact zone,
1335 and trackable for ≥ 20 sec. Scale bars, 2 μm. (**M**) The peak FI of an AF546-Fab' cluster was
1336 measured over time, and the increasing rate of AF546-Fab' peak FI of this cluster was
1337 determined by the slope of the plot. (**N-Q**) The rates (±SEM) of increase in AF546-Fab' peak FI
1338 in individual clusters were compared between during and after contraction (**N**), between B-cells
1339 treated with CK-689 and CK-666 from 0 min (**O**), between DMSO- and Wisko-treated B-cells
1340 (**P**), and between flox control and cNKO B-cells (**Q**) after B-cells reached maximal spreading.
1341 Data points represent individual cells, the averaged slopes of clusters detected in one B-cell,
1342 from 3 independent experiments with 6~12 cells per condition per experiment. *p <0.05, ** p
1343 <0.01, ***p<0.001, by non-parametric student's t-test.
1344 **Figure supplement 1.** Fab'-PLB, but not Tf-PLB, induces BCR clustering and phosphorylation.
1345 **Figure supplement 2.** Tracking and analyzing AF546-Fab' clusters in the B-cell contact zone.
1346 **Figure 6-Video 1.** Inhibition of B-cell contraction reduces the molecular density within BCR
1347 clusters.
1348

1349 **Figure 7. Increased molecular density in BCR clusters leads to reductions in BCR**
1350 **phosphorylation.** (**A-G**) Flox control and cNKO B-cells incubated with AF546-Fab'-PLB were
1351 fixed at 1, 3, 5, and 7 min, permeabilized, stained for phosphorylated CD79a (pCD79a,
1352 Tyr182), and imaged using TIRF and IRM. (**A**) Representative IRM and TIRF images of a flox
1353 control versus a cNKO B-cell at 7 min. Scale bars, 2 μm. (**B-D**) Ratios of pCD79a MFI relative to
1354 AF546-Fab' MFI were plotted against AF546-Fab' peak FI in individual AF546-Fab' clusters in
1355 the contact zone of flox control (**B**), cNKO B-cells (**C**), or flox control and cNKO B-cells overlay
1356 (**D**). AF546-Fab' clusters were identified as described in Figure 6 and Figure 6-figure
1357 supplement 2. Blue dots represent individual AF546-Fab' clusters with an equal number of
1358 clusters from the 4 time points. The black line and diamond symbols represent the average
1359 ratios of pCD79a MFI to Fab' MFI in individual BCR-Fab' clusters within the indicated Fab' peak
1360 FI range. The brown line and square symbols represent the fraction of the AF546-Fab' clusters
1361 out of the total, within the indicated Fab' peak FI range. Clusters were divided into three
1362 populations based on their peak AF546-Fab' FI, relatively low (<190), medium (190-280), and
1363 high (>280, detected only in contracted cells), and the pCD79a to AF546-Fab' MFI ratios of the
1364 three populations were compared (**B** and **C**). Data were generated from 3 independent
1365 experiments with ~20 cells and ≥125 clusters per condition per experiment. * p <0.05, ***
1366 p<0.001, by non-parametric student's t-test. The p-values in **D** were corrected using the
1367 Benjamini-Hochberg/Yekutieli method for false discovery rate control. (**E-G**) The MFI (±SEM) of
1368 AF546-Fab' (**E**) and pCD79a (**F**) and the MFI ratio (±SEM) of pCD79a relative to AF546-Fab'
1369 (**G**) in individual AF546-Fab' clusters at indicated times were compared between flox control and
1370 cNKO B-cells and between different times. (**H-K**) WT B-cells treated with CK-689 or CK-666
1371 after 2 min-incubation with AF546-Fab'-PLB. (**H**) Representative IRM and TIRF images of a CK-
1372 689- versus a CK-666-treated B-cell at 7 min. Scale bars, 2 μm. (**I-K**) The MFI (±SEM) of
1373 AF546-Fab' (**I**) and pCD79a (**J**) and the MFI ratio (±SEM) of pCD79a relative to AF546-Fab' (**K**)
1374 in individual AF546-Fab' clusters were compared between CK-689- and CK-666-treated B-cells

1375 after 7 min stimulation. Data points represent individual clusters. Horizontal solid lines in the
1376 violin plots represent the mean, while the dotted lines represent the quartiles of the distribution.
1377 Data were generated from 3 independent experiments with ~20 cells per condition per
1378 experiment. * p <0.05, *** p<0.001, by non-parametric student's *t*-test.
1379
1380 **Figure 8. Effects of BCR-Fab' density on the association of Syk with BCR-Fab' clusters**
1381 **and its phosphorylation.** Primary B-cells from flox control and cNKO mice were incubated with
1382 AF546-Fab'-PLB at 37°C, fixed at 3 or 7 min, stained for total Syk and phosphorylated Syk
1383 (pSyk Y519/520), and imaged by IRM and TIRF. (**A**) Representative IRM and TIRF images of
1384 Syk staining in a flox control versus a cNKO B-cell at 7 min (Scale bars, 2 μm). (**B-D**) Ratios of
1385 Syk MFI relative to AF546-Fab' MFI were plotted against AF546-Fab' peak IF in individual
1386 AF546-Fab' clusters in the contact zone of Flox control (**B**) and cNKO B-cells (**C**) and their
1387 overlay (**D**). AF546-Fab' clusters were identified as described in Figure 6 and Figure 6-figure
1388 supplement 2 from an equal number of cells after 3- and 7-min stimulation. Blue dots represent
1389 individual AF546-Fab' clusters with an equal number of clusters from each time point. The black
1390 line and diamond symbols represent the average ratios of Syk MFI to Fab' MFI in individual
1391 AF546-Fab' clusters at indicated Fab' peak FI ranges. The brown line and square symbols
1392 represent the fraction of the AF546-Fab' clusters out of the total at indicated Fab' peak FI
1393 ranges. (**E**) Representative IRM and TIRF images of pSyk staining in a flox control versus a
1394 cNKO B-cell at 7 min (Scale bars, 2 μm). (**F-H**) Ratios of pSyk MFI relative to AF546-Fab' MFI
1395 were plotted against AF546-Fab' peak IF in individual AF546-Fab' clusters in the contact zone
1396 of flox control (**F**) and cNKO B-cells (**G**) and their overlay (**H**). Blue dots represent individual
1397 AF546-Fab' clusters with an equal number of clusters from each time point. The black line and
1398 diamond symbols represent the average ratios of pSyk MFI to Fab' MFI in individual AF546-Fab'
1399 clusters at indicated Fab' peak FI ranges. The brown line and square symbols represent the
1400 fraction of the AF546-Fab' clusters out of the total at indicated Fab' peak FI ranges. (**I-K**) MFI

1401 ratios of pSyk relative to AF546-Fab' were plotted against AF546-Fab' peak IF in individual pSyk
1402 puncta in the contact zone of Flox control (**I**) and cNKO B-cells (**J**) and their overlay (**K**). pSyk
1403 puncta were identified using the criteria: FI ≥1.3 fold of the background outside the B-cell
1404 contact zone and diameter ≥250 nm. Blue dots represent individual pSyk puncta with an equal
1405 number of clusters from each time point. The black line and diamond symbols represent the
1406 average ratios of pSyk MFI to Fab' MFI in individual pSyk puncta at indicated Fab' peak FI
1407 ranges. The brown line and square symbols represent the fraction of the pSyk puncta out of the
1408 total at indicated Fab' peak FI ranges. Clusters were divided into three populations based on
1409 their peak AF546-Fab' FI, relatively low (<190), medium (190-280), and high (>280, detected
1410 only in contracted cells), and the Syk (**B** and **C**) or pSyk (**F**, **G**, **I**, and **J**) to AF546-Fab' MFI
1411 ratios of the three populations were compared. Data were generated from 3 independent
1412 experiments with ~23 cells and ≥125 clusters per condition per experiment. * p <0.05, ** p
1413 <0.01, *** p<0.001, by non-parametric student's *t*-test, between AF546-Fab' cluster group with
1414 different Fab' peak FI ranges. The *p*-values in **D, H,** and **K** were corrected using the Benjamini-
1415 Hochberg/Yekutieli method for false discovery rate control.
1416
1417 **Figure 9. The effects of BCR-Fab' density on the association of SHIP-1 with BCR-Fab'**
1418 **clusters and its phosphorylation.** Primary B-cells from flox control and cNKO mice were
1419 incubated with AF546-Fab'-PLB at 37ºC, fixed at 3 or 7 min, stained for total SHIP-1 and
1420 phosphorylated SHIP-1 (pSHIP-1 Tyr1020), and imaged by TIRF. (**A**) Representative IRM and
1421 TIRF images of SHIP-1 staining in a flox control versus a cNKO B-cell at 7 min (Scale bars, 2
1422 μm). (**B-D**) Ratios of SHIP-1 MFI relative to AF546-Fab' MFI were plotted against AF546-Fab'
1423 peak IF in individual AF546-Fab' clusters in the contact zone of Flox control (**B**) and cNKO B-
1424 cells (**C**). An overlay of flox control and cNKO plots is also shown (**D**). AF546-Fab' clusters were
1425 identified as described in Figure 6 and Figure 6-figure supplement 2 from an equal number of

1426 cells after 3 and 7 min stimulation. Blue dots represent individual AF546-Fab' clusters with an
1427 equal number of clusters from each time point. The black line and diamond symbols represent
1428 the average ratios of SHIP-1 MFI to Fab' MFI in individual AF546-Fab' clusters at indicated Fab'
1429 peak FI ranges. The brown line and square symbols represent the fraction of the AF546-Fab'
1430 clusters out of the total at indicated Fab' peak FI ranges. (**E**) Representative IRM and TIRF
1431 images of pSHIP-1 staining in a flox control versus a cNKO B-cell at 7 min (Scale bars, 2 μm).
1432 (**F-H**) Ratios of pSHIP-1 MFI relative to AF546-Fab' MFI were plotted against AF546-Fab' peak
1433 IF in individual AF546-Fab' clusters in the contact zone of flox control **(F)** and cNKO B-cells (**G**)
1434 and their overlay (**H**). Blue dots represent individual AF546-Fab' clusters with an equal number
1435 of clusters from each time point. The black line and diamond symbols represent the average
1436 ratios of pSHIP-1 MFI to Fab' MFI in individual AF546-Fab' clusters at indicated Fab' peak FI
1437 ranges. The brown line and square symbols represent the fraction of the AF546-Fab' clusters
1438 out of the total at indicated Fab' peak FI ranges. (**I-K**) MFI ratios of pSHIP-1 relative to AF546-
1439 Fab' were plotted against AF546-Fab' peak IF in individual pSHIP-1 puncta in the contact zone
1440 of Flox control **(I)** and cNKO B-cells (**J**) and their overlay (**K**). pSHIP-1 puncta were identified
1441 using the criteria: FI ≥1.5 fold of the background outside the B-cell contact zone and diameter
1442 ≥250 nm. Blue dots represent individual pSHIP-1 puncta with an equal number of clusters from
1443 each time point. The black line and diamond symbols represent the average ratios of pSHIP-1
1444 MFI to Fab' MFI in individual pSHIP-1 puncta at indicated Fab' peak FI ranges. The brown line
1445 and square symbols represent the fraction of the total pSHIP-1 puncta at indicated Fab' peak FI
1446 ranges. Clusters were divided into three populations based on their peak AF546-Fab' FI,
1447 relatively low (<200), medium (200-300), and high (>300, detected only in contracted cells), and
1448 the SHIP-1 (**B** and **C**) or pSHIP-1 (**F**, **G**, **I**, and **J**) to AF546-Fab' MFI ratios of the three
1449 populations were compared. Data were generated from 3 independent experiments with ~23
1450 cells and ≥125 clusters per condition per experiment. * p <0.05, ** p <0.01, *** p<0.001, by non-

1451 parametric student's *t*-test, between AF546-Fab' cluster group with different Fab' peak FI
1452 ranges. The *p*-values in **D, H,** and **K** were corrected using the Benjamini-Hochberg/Yekutieli
1453 method for false discovery rate control.
1454
1455 **Figure 10. A working model for cell traction-mediated BCR signaling attenuation.** When
1456 encountering membrane-associated antigen, mature follicular B-cells undergo rapid spreading,
1457 primarily driven by WASP-mediated branched actin polymerization, which maximizes B-cell
1458 contact with antigen-presenting surface and BCR-antigen engagement, amplifying signaling.
1459 Upon reaching maximal spreading, N-WASP distal to lamellipodial networks activates Arp2/3-
1460 mediated branched actin polymerization, which initiates the generation of inner F-actin foci from
1461 lamellipodia towards the center of the B-cell contact zone. NMII is then preferentially recruited to
1462 these relatively stable inner foci, which in turn promotes the centripetal movement of inner F-
1463 actin foci and the maturation of ring-like actomyosin structures, enabling B-cell contraction. B-
1464 cell contraction pushes the BCR microclusters formed during B-cell spreading to the center of
1465 the contact zone, increasing their molecular density. Increased molecular density promotes the
1466 disassociation of signaling molecules from BCR clusters, probably due to crowding and
1467 conformational changes, leading to signaling attenuation.
1468

Figure 1

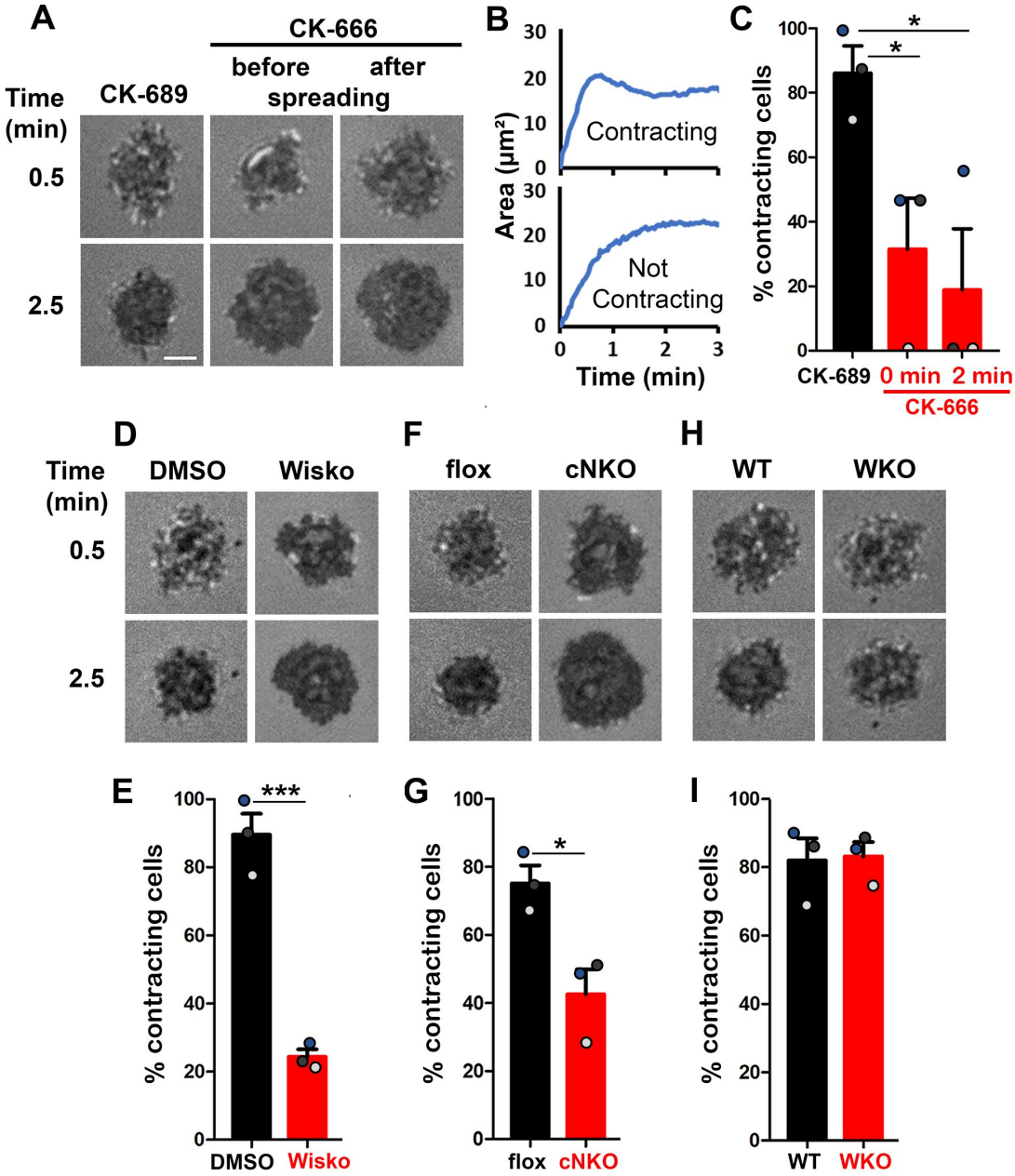

1469

Figure 2

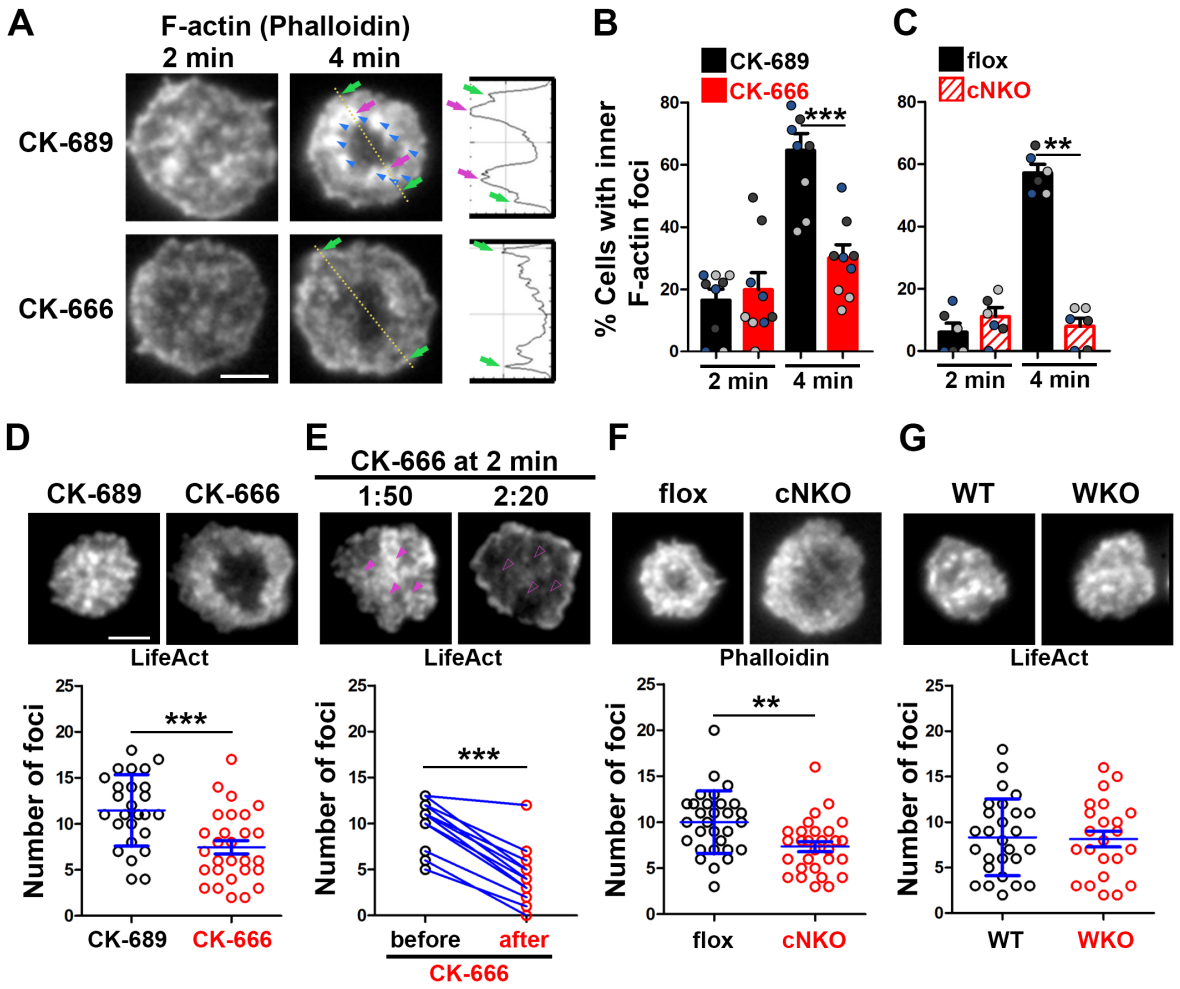

1470

Figure 3

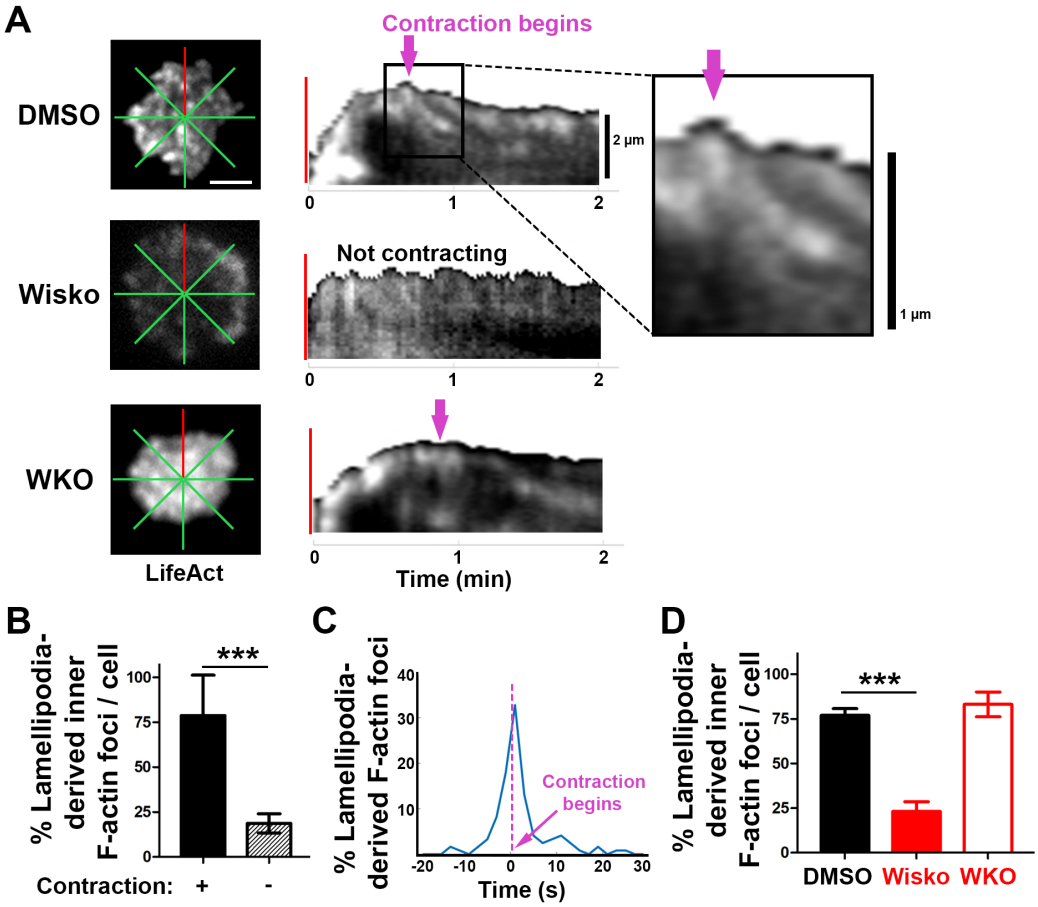

1471

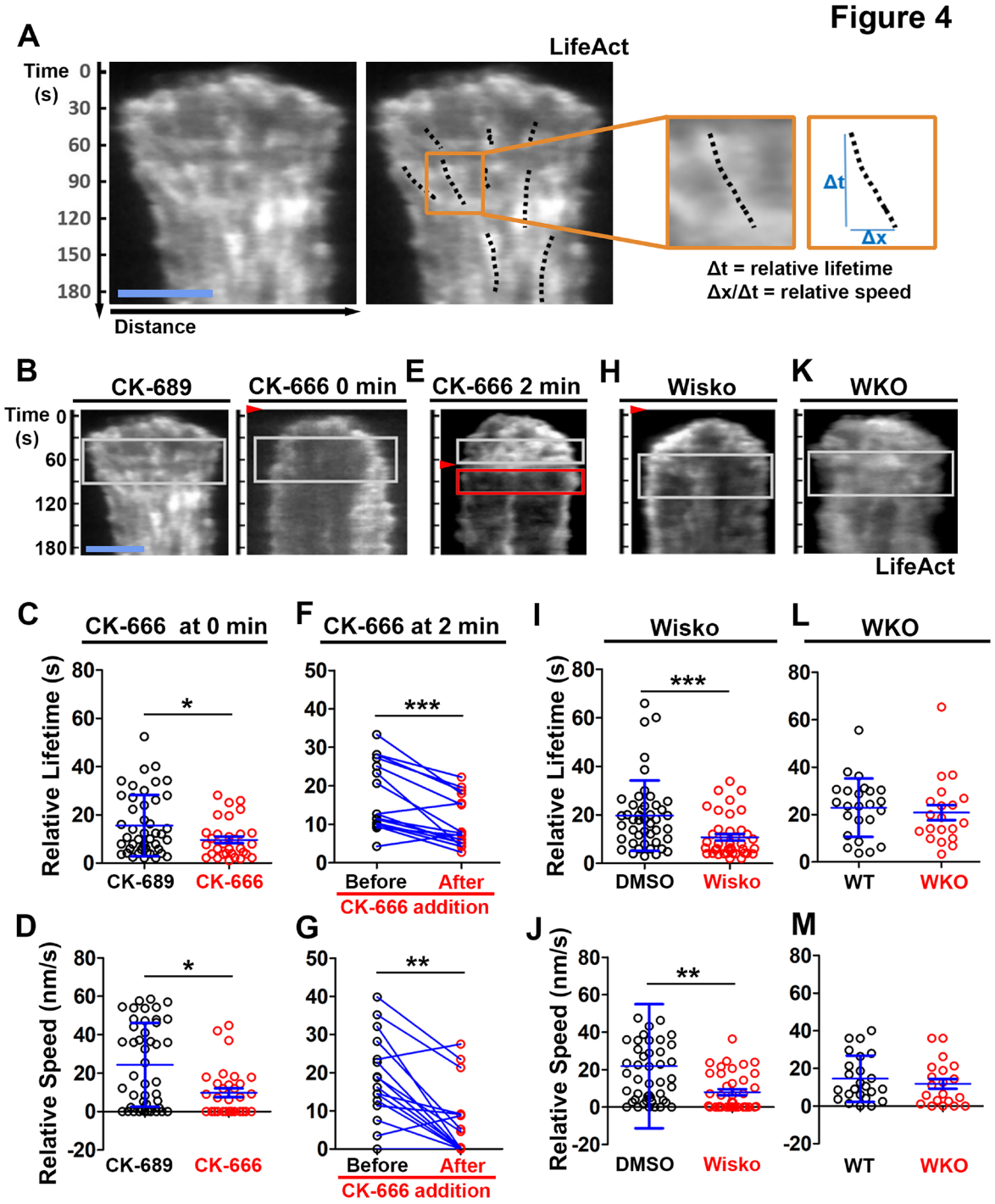
Figure 4
A
LifeAct
Time (s)
0
30
60
90
120
150
180
Distance
Δt
Δx
Δt = relative lifetime
Δx/Δt = relative speed
B
CK-689
CK-666 0 min
E
CK-666 2 min
H
Wisko
K
WKO
LifeAct
C
CK-666 at 0 min
Relative Lifetime (s)
CK-689
CK-666
F
CK-666 at 2 min
Before
After
CK-666 addition
I
Wisko
DMSO
Wisko
L
WKO
WT
WKO
D
Relative Speed (nm/s)
G
J
M

1472

Figure 5

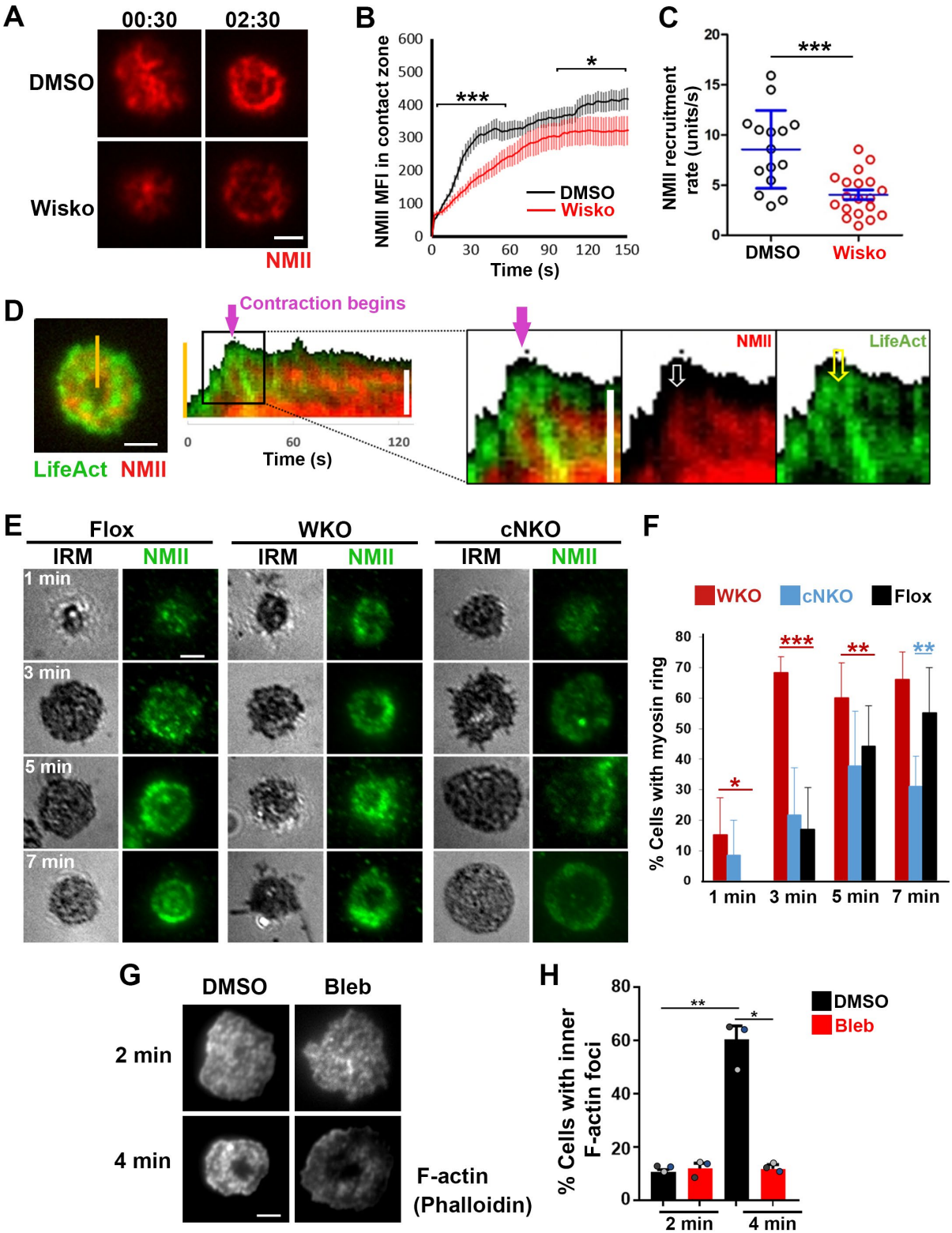

1473

Figure 6

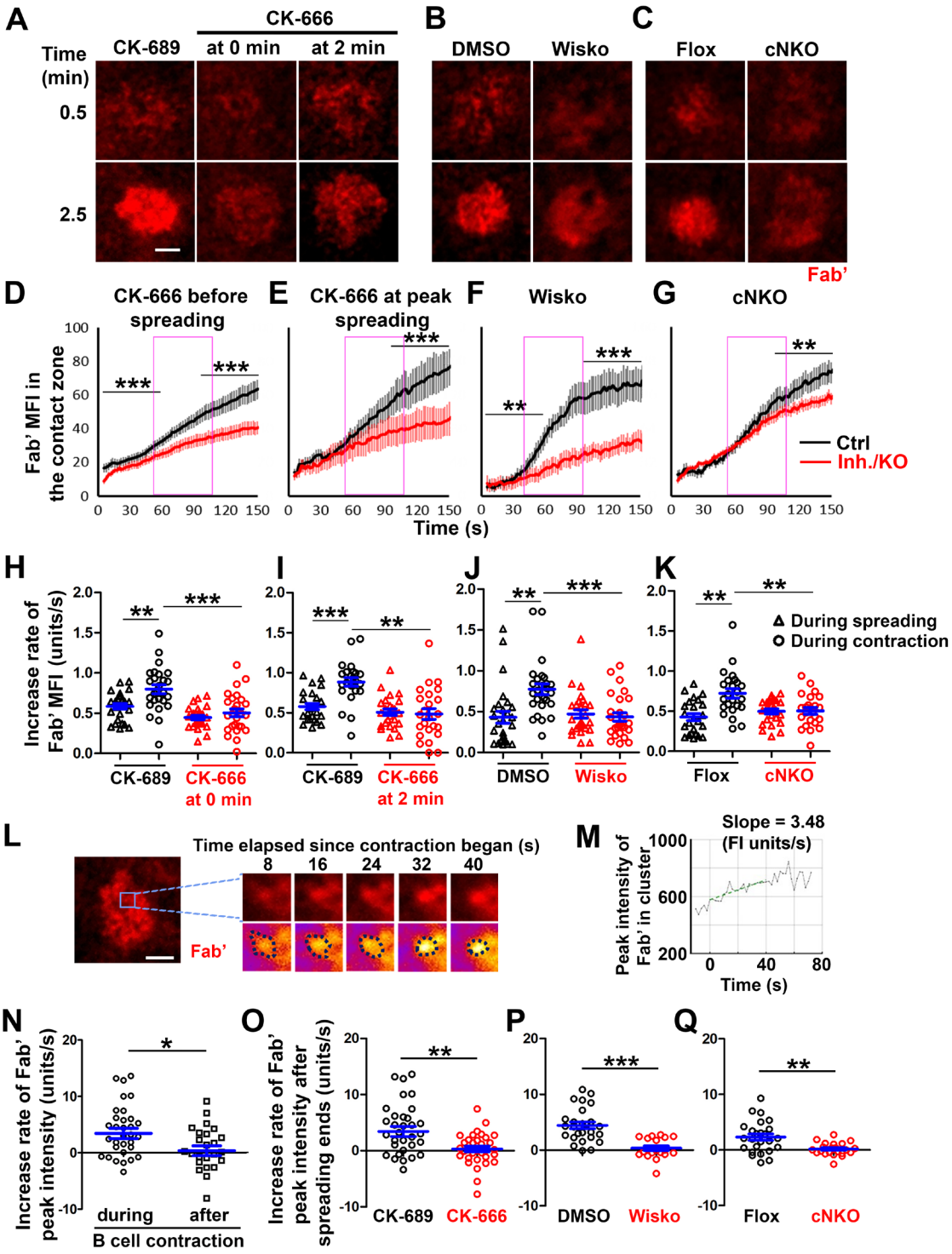

1474

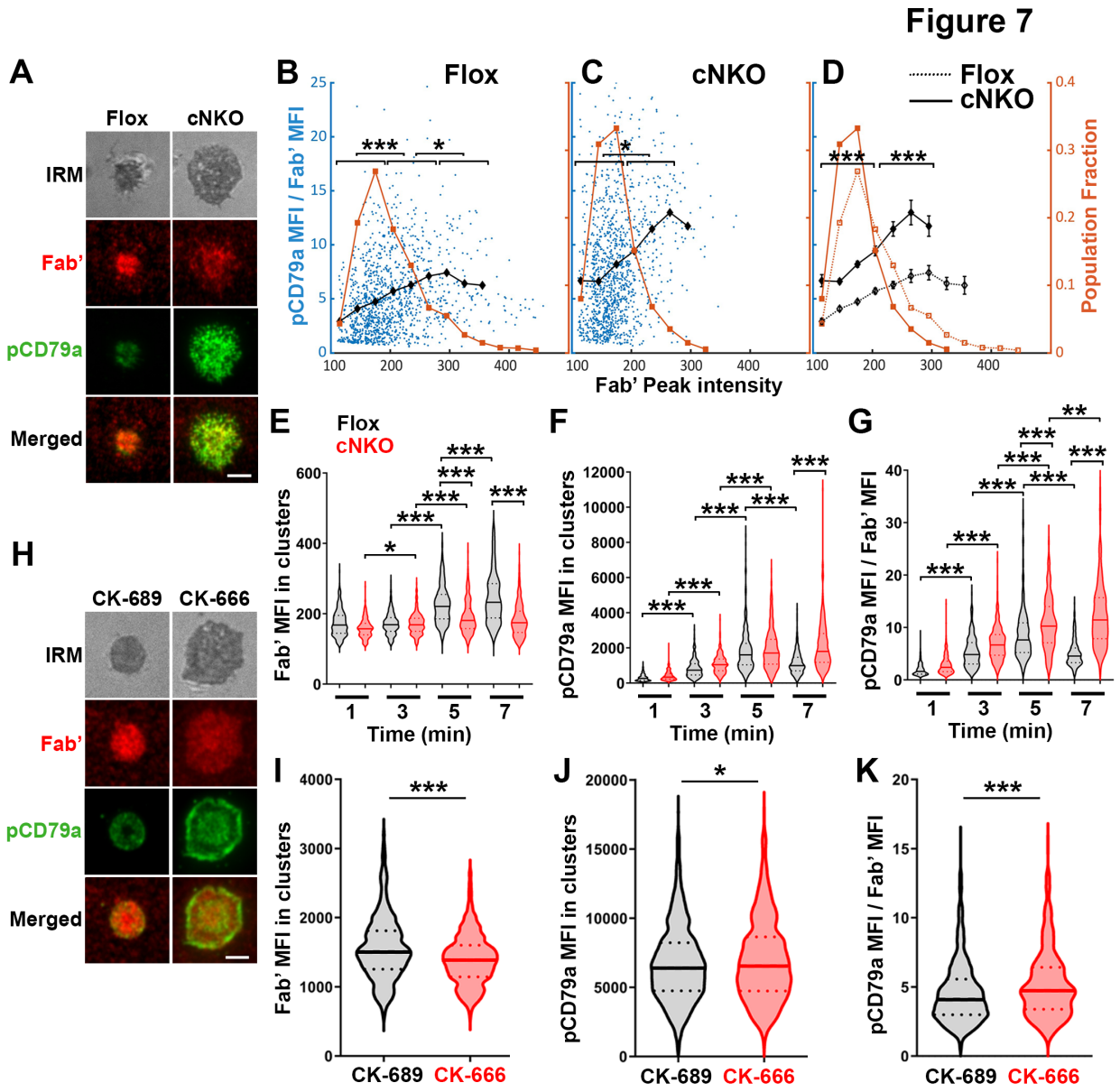
Figure 7
A
Flox
cNKO
IRM
Fab'
pCD79a
Merged
B
Flox
C
cNKO
D
Flox
cNKO
pCD79a MFI / Fab' MFI
Population Fraction
Fab' Peak intensity
E
Flox
cNKO
Fab' MFI in clusters
Time (min)
F
pCD79a MFI in clusters
Time (min)
G
pCD79a MFI / Fab' MFI
Time (min)
H
CK-689
CK-666
IRM
Fab'
pCD79a
Merged
I
Fab' MFI in clusters
CK-689
CK-666
J
pCD79a MFI in clusters
CK-689
CK-666
K
pCD79a MFI / Fab' MFI
CK-689
CK-666

1475

Figure 8

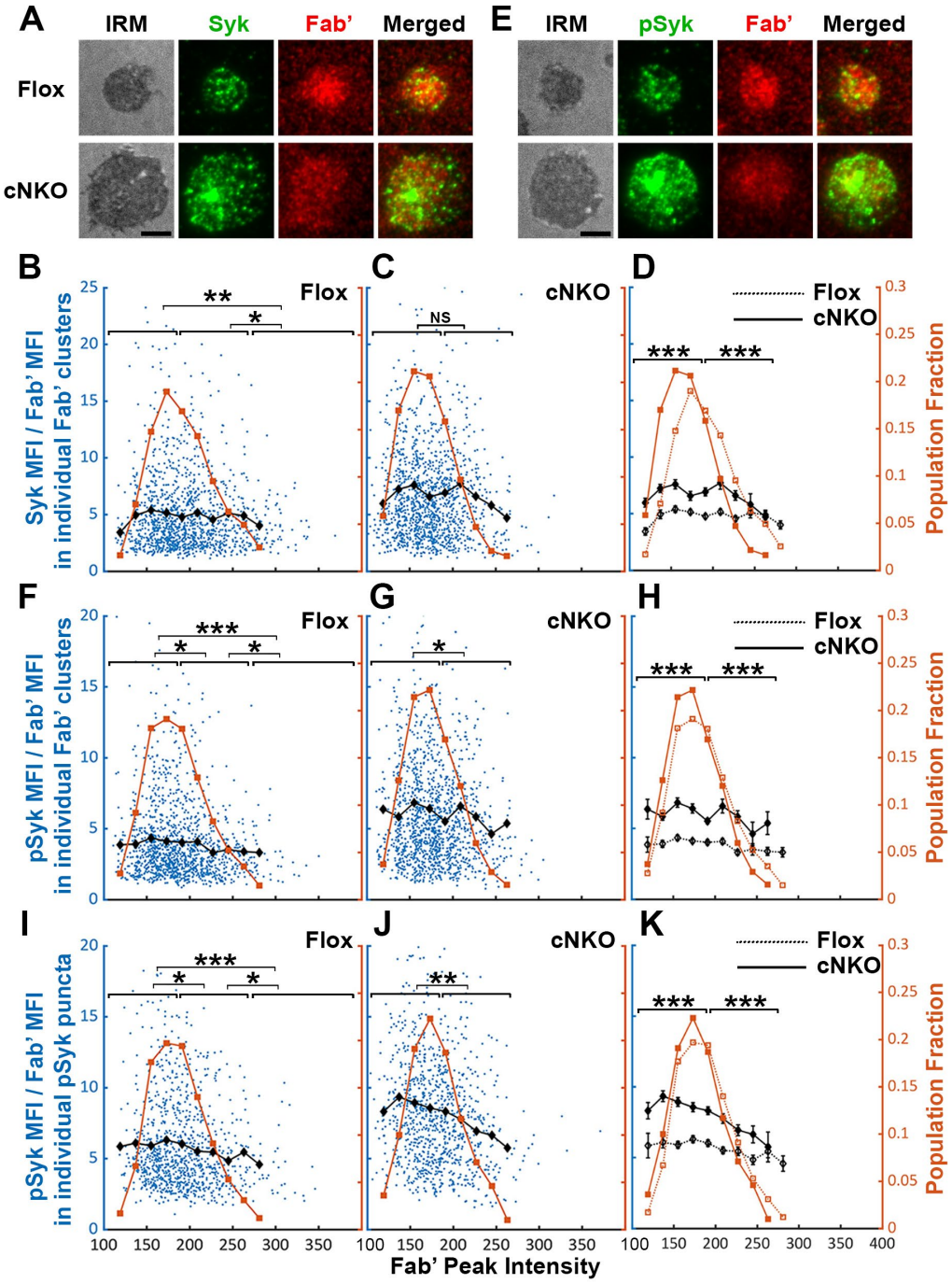

1476

Figure 9

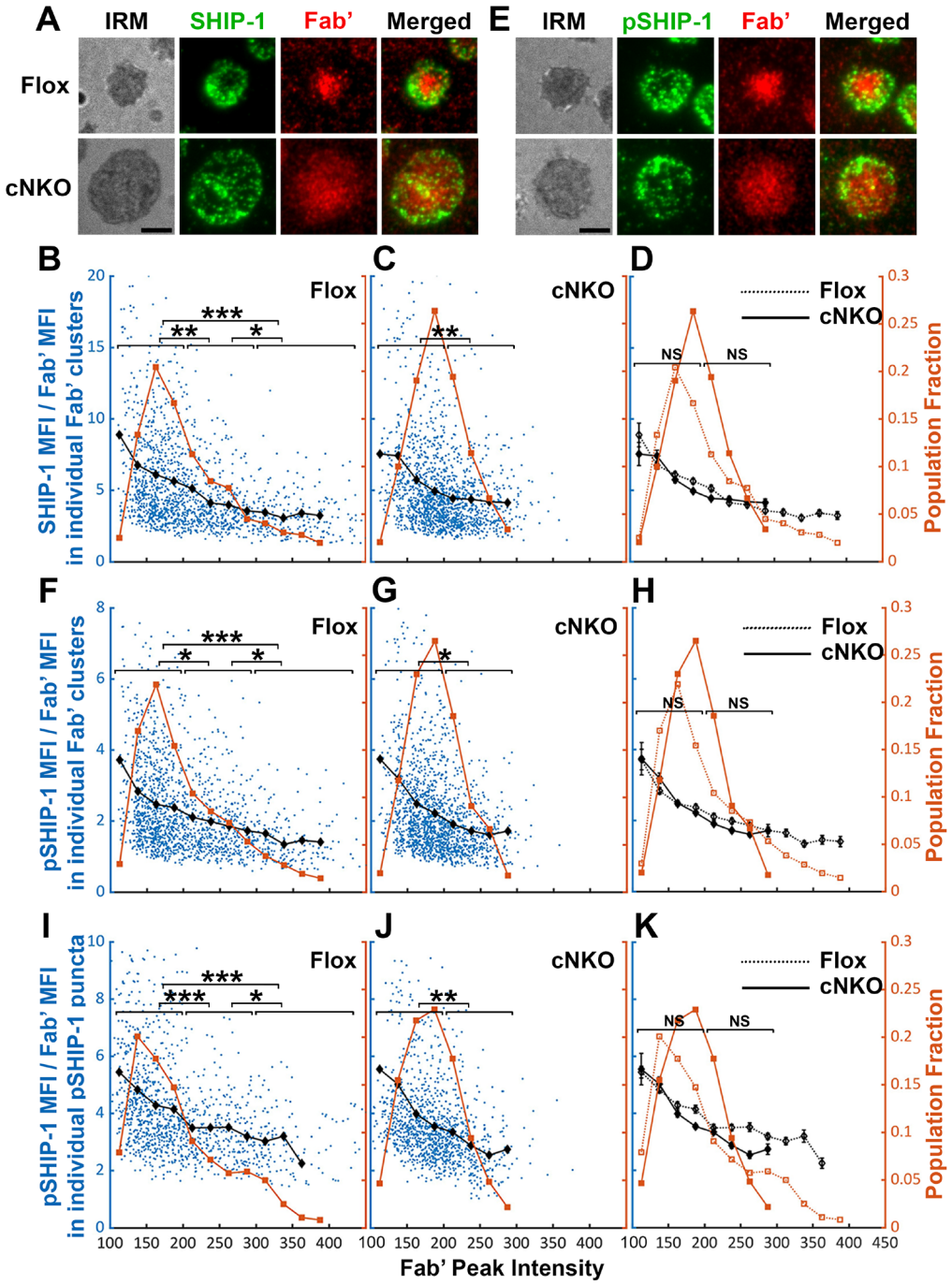

1477

Figure 10

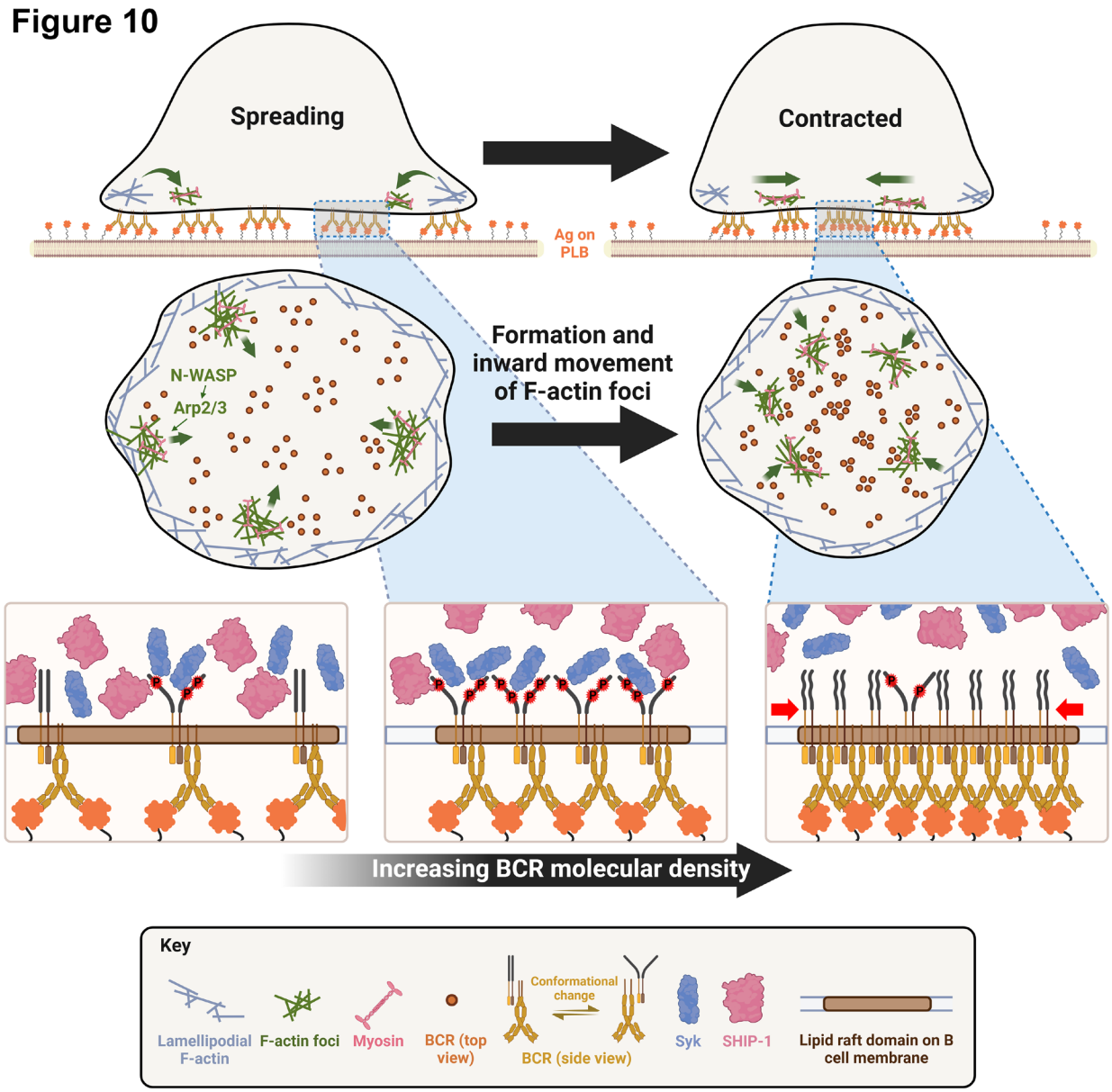

1478

1479 **Supplementary materials for this manuscript include the following:**

1480 7 figures

1481 4 videos

Figure 1-S1

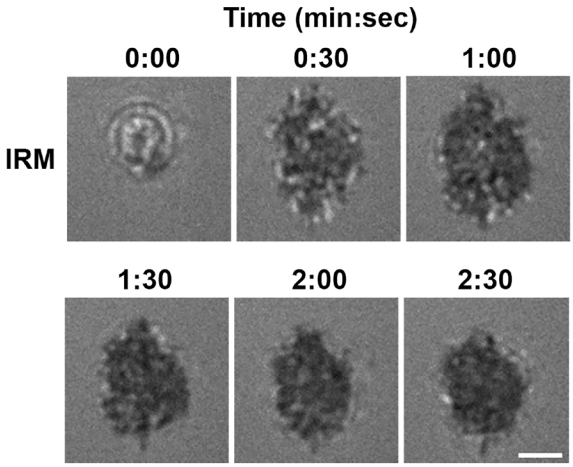

1482

1483 **Figure 1-figure supplement 1. B-cells spread and contract on Fab'-coated-planar lipid**
1484 **bilayers.** Splenic B-cells were pre-warmed to 37°C and incubated with planar lipid bilayers
1485 coated with monobiotinylated Fab' fragment of goat anti-mouse IgG+M (Fab'-PLB) and imaged
1486 live at 37°C by interference reflection microscopy (IRM). Shown are individual frames from a
1487 time-lapse IRM image of one B-cell. The plasma membrane area contacting with Fab'-PLB (B-
1488 cell contact zone) visualized by IRM increased between 0-1 min after landing, indicating
1489 spreading, and decreased after 1 min 30 sec, indicating contraction. Scale bar, 2 μm.

Figure 1-S2

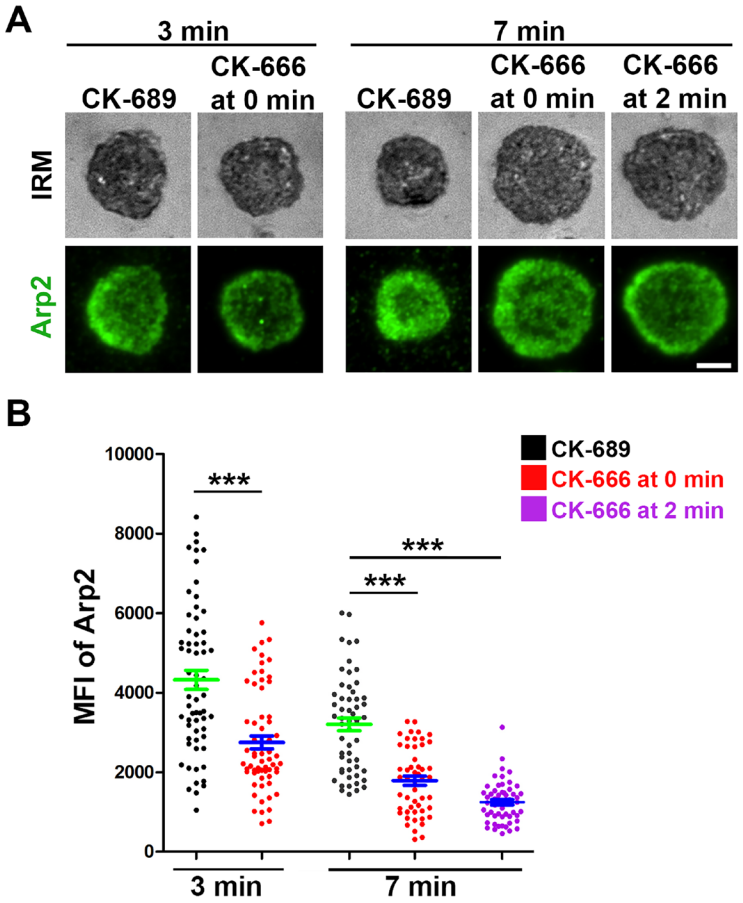

1490

1491 **Figure 1-figure supplement 2. CK-666 significantly decreases Arp2/3 recruitment to the B-**

1492 **cell contact zone.** WT splenic B-cells were treated with CK-689 or CK-666 (50 μM) before (0

1493 min) and after maximal spreading (2 min) during incubation with Fab'-PLB at 37°C. Cells were

1494 fixed at 3 and 7 min, permeabilized, stained for Arp2, and imaged using IRM and TIRF. Shown

1495 are representative images (**A**) and the MFI of Arp2 in the contact zone at 3 min and 7 min

1496 compared between B-cell treated with CK-689 (black dots), CK-666 from 0 min (red dots), and

1497 CK-666 from 2 min (purple dots) (**B**). Data points represent individual cells from 3 independent

1498 experiments with ~20 cells per condition per experiment. Scale bar, 2 μm. *** $p<0.001$, by non-

1499 parametric student's *t*-test.

Figure 1-S3

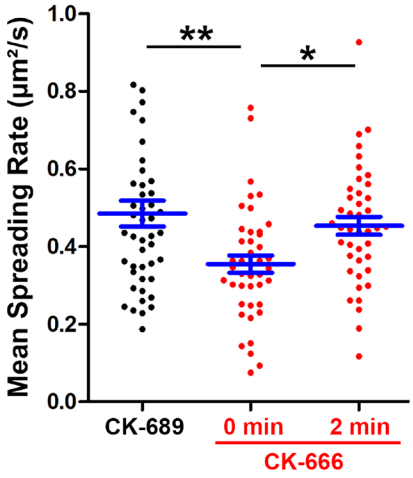

1500

1501 **Figure 1-figure supplement 3. CK-666 treatment before but not after maximal B-cell**

1502 **spreading decreased the spreading kinetics.** WT splenic B-cells were treated with CK-689 or

1503 CK-666 (50 μM) before (0 min) and after maximal spreading (2 min) during incubation with Fab'-

1504 PLB and imaged live at 37°C by IRM. The area occupied by the B-cell contact zone was

1505 measured using IRM images and custom codes made in MATLAB. The mean spreading rate of

1506 each cell during its early spreading phase was quantified using the contact area versus the time

1507 curve of that cell by linear regression. The averaged spreading rates (±SEM) were generated

1508 from 3 independent experiments with ~15 cells per condition per experiment. * $p>0.05$, **

1509 $p<0.01$, by non-parametric student's *t*-test.

Figure 1-S4

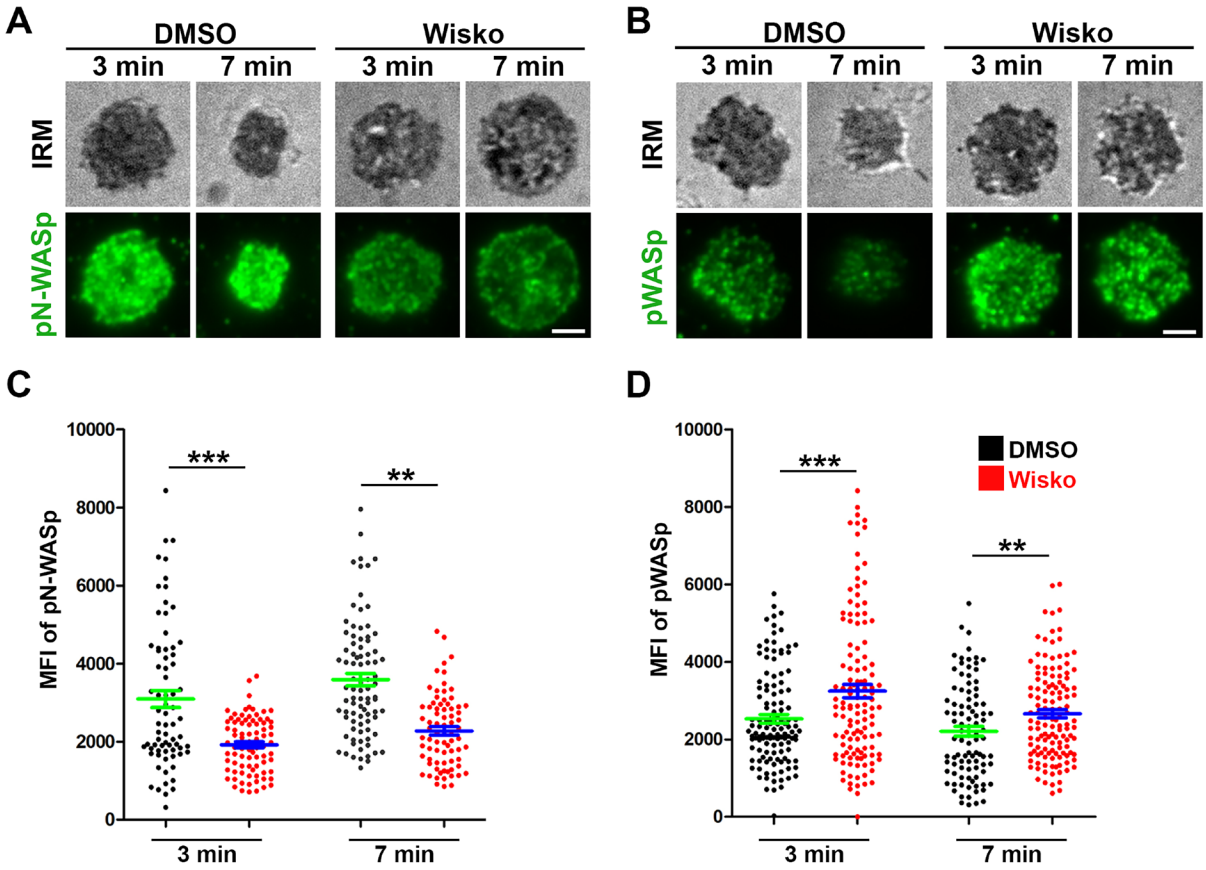

1510

1511 **Figure 1-figure supplement 4. Wiskostatin treatment inhibits N-WASP activation while**
1512 **enhancing WASP activation in B-cells.** WT splenic B-cells were pre-treated with Wiskostatin
1513 (Wisko, 10 μM) or DMSO (control) for 10 min at 37ºC before and during incubation with Fab'-
1514 PLB. Cells were fixed at 3 and 7 min, permeabilized, stained for phosphorylated N-WASP (pN-
1515 WASP) or WASP (pWASP), and imaged using IRM and TIRF. Shown are representative IRM
1516 and TIRF images of pN-WASP (**A**) and pWASP (**B**) at the B-cell contact zone and the MFI
1517 (±SEM) of pN-WASP (**C**) and pWASP (**D**) in the B-cell contact zone, comparing between DMSO
1518 and Wisko-treated B-cells. Data points represent individual cells from 3 independent
1519 experiments with ~25 cells per condition per experiment. Scale bar, 2 μm. ** $p<0.01$, ***
1520 $p<0.001$, by non-parametric student's *t*-test.

Figure 3-S1

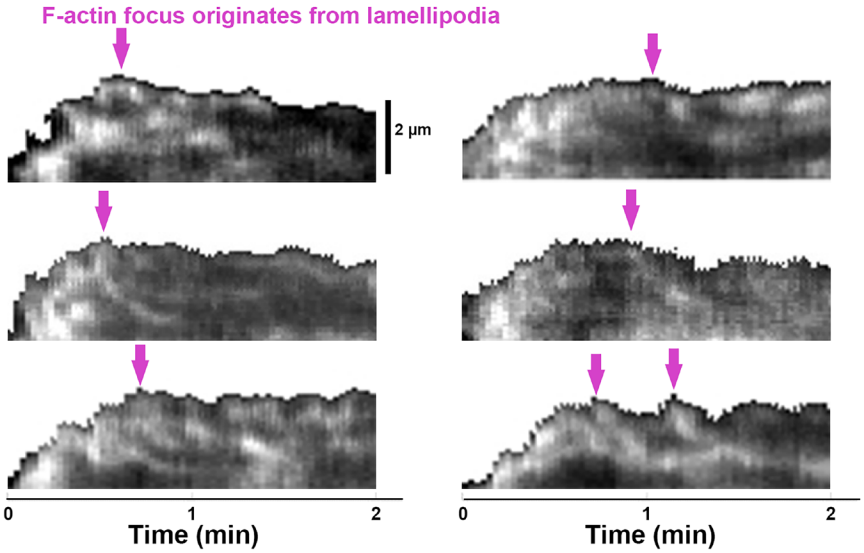

1521

1522 **Figure 3-figure supplement 1. Emerging of Inner F-actin foci from lamellipodia.** Splenic B-
1523 cells from LifeAct-GFP transgenic mice were treated with DMSO, imaged live using TIRF and
1524 IRM during incubation with Fab'-PLB at 37°C, and analyzed using kymographs that were
1525 randomly generated from each cell. Shown are six examples of the kymographs used for
1526 analysis. Arrows indicate the emergence of inner F-actin foci near the lamellipodia.
1527 Lamellipodia-derived inner F-actin foci were identified by their LifeAct-GFP FI ≥2 fold of their
1528 nearby region, inside location in the contact zone, migrating away the lamellipodial F-actin, and
1529 trackable for ≥8 sec.

1530

Figure 6-S1

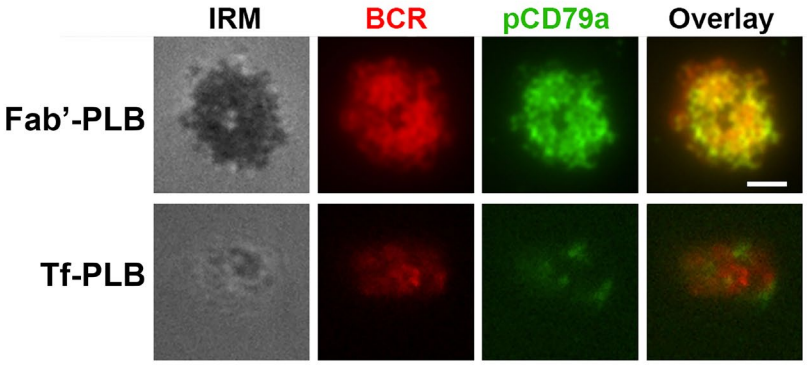

1531

1532 **Figure 6-figure supplement 1. Fab'-PLB, but not Tf-PLB, induces BCR clustering and**

1533 **phosphorylation.** WT splenic B-cells were pre-labeled with Cy3-Fab fragment of goat anti-

1534 mouse IgM+G at a concentration of 2.5 µg per 10^6 cells at 4°C for 30 min, followed by

1535 incubation with Fab'-PLBs or Tf-PLBs for 5 min at 37°C. Cells were fixed, permeabilized,

1536 stained for pCD79a, and imaged using IRM and TIRF. Shown are representative IRM and TIRF

1537 images from three independent experiments. Scale bar, 2 µm.

Figure 6-S2

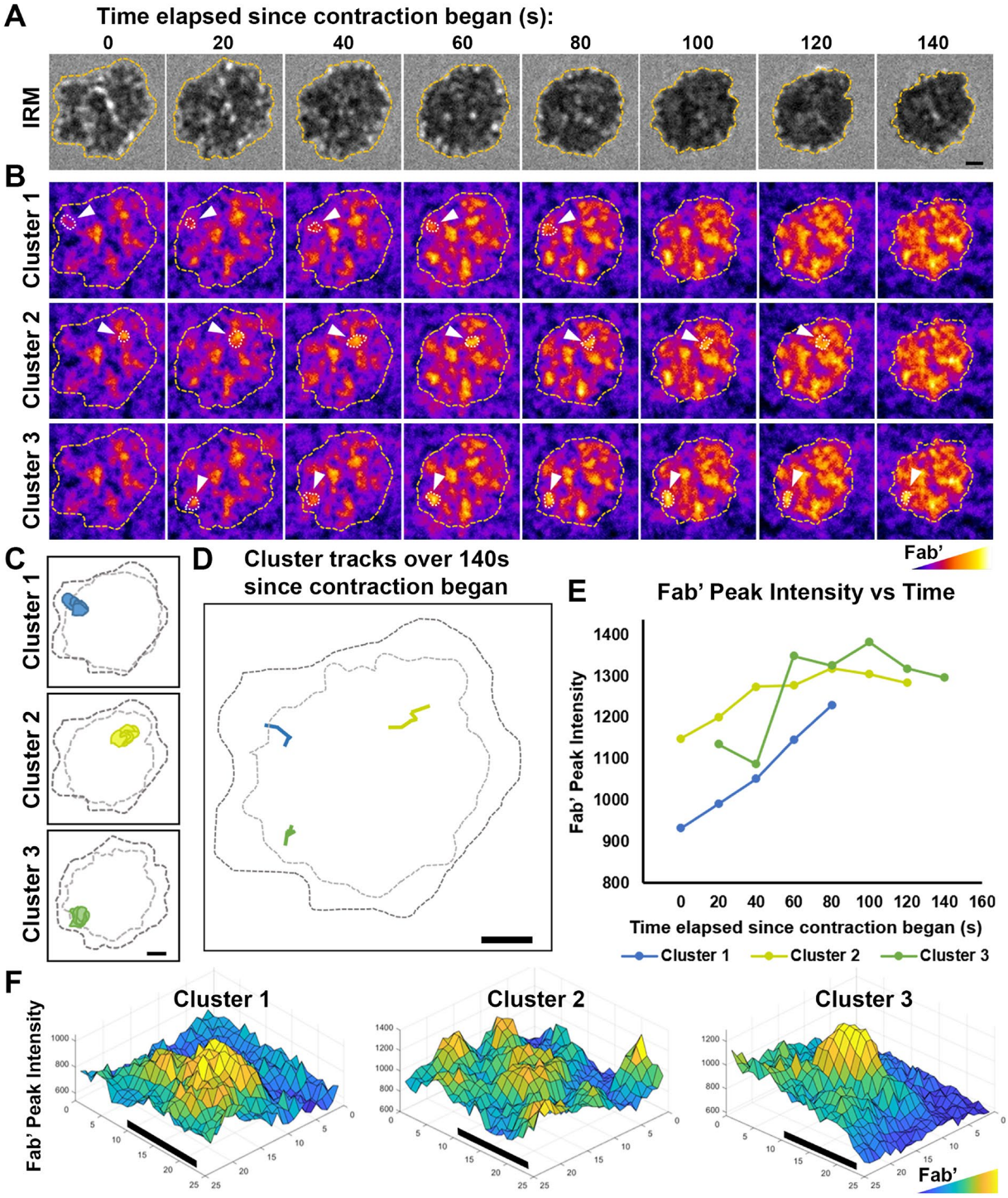

1538

1539 **Figure 6-figure supplement 2. Tracking and analyzing AF546-Fab' clusters in the B-cell**
1540 **contact zone.** WT splenic B-cells were incubated with AF546-Fab'-PLB at 37°C and imaged
1541 live using IRM and TIRF. Shown are individual frames from time-lapse images of IRM (**A**) and
1542 TIRF (**B**), showing AF546-Fab' clusters within the contact zone of one DMSO-treated (vehicle
1543 control for Wisko) B-cell for 140 sec since the beginning of contraction. Fab' FI is shown as heat
1544 maps using NIH ImageJ. The boundary of the contact zone, detected using IRM images by a
1545 custom MATLAB script, is shown in yellow dashed lines. Arrows point to three representative
1546 clusters among the other clusters detected in the contact zone using custom MATLAB codes.
1547 Cluster detection masks for the three representative clusters are shown (**C**). Moving tracks for
1548 the three AF546-Fab' clusters are shown alongside the initial (black dashed lines) and final state
1549 (gray dashed lines) of the contact zone (**D**). Tracks were generated by following the peak of
1550 AF546 FI in each cluster as it moved. AF546-Fab' peak FI versus time curves for the three
1551 representative clusters are plotted over the duration that each cluster could be detected (**E**).
1552 Surface plots (2.5-D plots) of AF546-Fab' FI show a zoomed-in region consisting of each of the
1553 three AF546-Fab' clusters (**F**). Colors in (**B**) and (**F**) are scaled to AF546-Fab' FI values. Scale
1554 bars, 1 μm.

1555 **Video Legends**

1556 **Figure 1-Video 1. Effects of CK-666, Wiskostatin, conditional N-WASP knockout, and**
1557 **WASP knockout on B-cell contraction.** Splenic B-cells were incubated with planar lipid
1558 bilayers coated with monobiotinylated Fab' fragment of goat anti-mouse IgG+M (Fab'-PLB) in
1559 the absence and presence of various inhibitors and imaged live at 37ºC at one frame per 2
1560 seconds by interference reflection microscopy (IRM). Shown are representative IRM time-lapse
1561 images of WT B-cells treated with CK-689 or CK-666 (50 μM) before (0 min) and after maximal
1562 spreading (2 min) (**A**), WT B-cells treated with DMSO or Wiskostatin (Wisko, 10 μM) 10 min
1563 before and during incubation with Fab'-PLB (**B**), B-cells from flox control and B-cell-specific N-
1564 WASP knockout (cNKO) mice (**C**), and B-cells from WT or WASP knockout mice (WKO) (**D**).
1565 The frame in which the contact zone first appears was considered time 0. The videos are sped
1566 up by 20x compared to real time. Scale bar, 2 μm.

1567

1568 **Figure 2-Video 1. Effects of CK-666 and WKO on F-actin foci formation.** Splenic B-cells
1569 from LifeAct-GFP transgenic mice were incubated with Fab'-PLB in the absence and presence
1570 of CK-689 or CK-666 and imaged live at 37ºC at one frame per 2 seconds by IRM and total
1571 internal reflection fluorescence microscopy (TIRF). Shown are representative IRM (**A** and **C**)
1572 and TIRF (**B** and **D**) time-lapse images of WT B-cells treated with CK-689 or CK-666 (50 μM)
1573 before and after maximal spreading (**A** and **B**) and WT and WKO B-cells expressing LifeAct-
1574 GFP (**C** and **D**). The video is sped up by 20x compared to real time. Scale bar, 2 μm.

1575

1576 **Figure 5-Video 1. Wiskostatin treatment inhibits NMII ring-like structure formation.** B-cells
1577 from mice expressing GFP fusion of non-muscle myosin IIA (GFP-NMIIA) and LifeAct-RFP
1578 transgenes were treated with DMSO or Wisko (10 μM) 10 min before and during incubation with
1579 Fab'-PLB. The B-cell contact zones were imaged live at one frame per 2 seconds using IRM

1580 and TIRF. Shown are representative IRM and TIRF time-lapse images. The video is sped up by
1581 20x compared to real time. Scale bar, 2 μm.
1582
1583 **Figure 6-Video 1. Inhibition of B-cell contraction reduces the molecular density within**
1584 **BCR clusters.** Splenic B-cells were incubated with AF546-Fab'-PLB in the absence and
1585 presence of various inhibitors and imaged live at 37°C at one frame per 2 seconds by IRM and
1586 TIRF. Shown are representative IRM **(A, C,** and **E)** and TIRF **(B, D,** and **F)** time-lapse images of
1587 WT B-cells treated with CK-689 or CK-666 (50 μM) before and after maximal spreading (**A** and
1588 **B**), WT B-cells treated with DMSO or Wisko (10 μM) 10 min before and during incubation with
1589 Fab'-PLB (**C** and **D**), and flox control or cNKO B-cells (**E** and **F**). TIRF images (**B, D,** and **F**) are
1590 shown as AF546-Fab' FI maps. The video is sped up by 20x compared to real time. Scale bar, 2
1591 μm.